PLOS COMPUTATIONAL BIOLOGY

RESEARCH ARTICLE

The Na^+/K^+-ATPase generically enables deterministic bursting in class I neurons by shearing the spike-onset bifurcation structure

Mahraz Behbood[1,2], **Louisiane Lemaire**[1,2], **Jan-Hendrik Schleimer**[1,2], **Susanne Schreiber**[1,2]*

1 Institute for Theoretical Biology, Department of Biology, Humboldt-Universität zu Berlin, Berlin, Germany, **2** Bernstein Center for Computational Neuroscience, Berlin, Germany

* s.schreiber@hu-berlin.de

Citation: Behbood M, Lemaire L, Schleimer J-H, Schreiber S (2024) The Na^+/K^+-ATPase generically enables deterministic bursting in class I neurons by shearing the spike-onset bifurcation structure. PLoS Comput Biol 20(8): e1011751. https://doi.org/10.1371/journal.pcbi.1011751

Editor: Kim T. Blackwell, The University of Iowa College of Engineering, UNITED STATES OF AMERICA

Received: December 11, 2023

Accepted: August 2, 2024

Published: August 12, 2024

Data Availability Statement: All codes and files required for reproducing the figures of this manuscript are available on Zenodo (DOI: 10.5281/zenodo.11385326) and also on Gitlab repository (https://itbgit.biologie.hu-berlin.de/compneurophys/the-na-k-atpase-generically-enables-deterministic-bursting-in-class-i-neurons-by-shearing-the-spike-onset-bifurcation-structure).

Funding: This project has received funding from the European Research Council (ERC) under the

Abstract

Slow brain rhythms, for example during slow-wave sleep or pathological conditions like seizures and spreading depolarization, can be accompanied by oscillations in extracellular potassium concentration. Such slow brain rhythms typically have a lower frequency than tonic action-potential firing. They are assumed to arise from network-level mechanisms, involving synaptic interactions and delays, or from intrinsically bursting neurons. Neuronal burst generation is commonly attributed to ion channels with slow kinetics. Here, we explore an alternative mechanism generically available to all neurons with class I excitability. It is based on the interplay of fast-spiking voltage dynamics with a one-dimensional slow dynamics of the extracellular potassium concentration, mediated by the activity of the Na^+/K^+-ATPase. We use bifurcation analysis of the complete system as well as the slow-fast method to reveal that this coupling suffices to generate a hysteresis loop organized around a bistable region that emerges from a saddle-node loop bifurcation–a common feature of class I excitable neurons. Depending on the strength of the Na^+/K^+-ATPase, bursts are generated from pump-induced shearing the bifurcation structure, spiking is tonic, or cells are silenced via depolarization block. We suggest that transitions between these dynamics can result from disturbances in extracellular potassium regulation, such as glial malfunction or hypoxia affecting the Na^+/K^+-ATPase activity. The identified minimal mechanistic model outlining the sodium-potassium pump's generic contribution to burst dynamics can, therefore, contribute to a better mechanistic understanding of pathologies such as epilepsy syndromes and, potentially, inform therapeutic strategies.

Author summary

The brain can produce slow rhythms, such as those observed during sleep or epilepsy. These rhythms are much slower than the neuronal electrical signals, and their origins are still under debate. Mechanisms discussed so far are often based on the connection delays in neural networks or on neuronal ion channels with particularly slow kinetics. We show that neurons with specific spiking dynamics–allowing them to fire at arbitrarily low

Union's Horizon 2020 research an innovation program (to SS, grant agreement no 864243), from the Einstein Foundation Berlin (to SS, EP-2021-621) and from the German Research Council (to SS FOR 5289, CRC/TRR 384). The funders had no role in study design, data collection and analysis, decision to publish, or preparation of the manuscript.

Competing interests: The authors have declared that no competing interests exist.

frequencies (so-called class I neurons) can produce slow rhythmic patterns without requiring synaptic connectivity or special ion channels. In these cells, slow rhythmic activity arises from the interplay of slow changes in extracellular potassium concentration and the cell's voltage dynamics, mediated by the Na^+/K^+-ATPase pump. The latter, found in all neurons, regulates the concentrations of sodium and potassium ions across the cell membrane. The core mechanism is not idiosyncratic, rather mathematical analysis shows under which conditions slow rhythmic activity can arise generically from the pump-based coupling in a broad class of neurons. We demonstrate that the pump is relevant for the creation of different firing patterns, some of which have been associated with pathologies of the brain. A better mechanistic understanding of these complex, concentration-dependent dynamics can therefore be relevant for therapeutic approaches.

Introduction

Rhythms on diverse timescales are a hallmark of our brain's activity. Such oscillatory activity is associated with physiological states, ranging from normal breathing to the consolidation of memories, or pathological situations such as epileptic seizures and spreading depolarization (SD) [1–5]. Some rhythms are orders of magnitude slower than single-neuron spiking. For these, different mechanistic origins of their slow dynamics have been proposed. First, a neuron's embedding in the network can produce bursts via reverberating activity, with synaptic delays serving as an important parameter that determines the period of the resulting oscillations [6]. Second, one or more cells with intrinsically bursting dynamics can act as pacemakers [7] and entrain larger networks. Combinations of both of the above mechanisms, network effects and intrinsic bursting, have also been reported [8]. Along these lines, brain regions that exhibit large-scale oscillatory behaviour often contain significant numbers of single-neuron bursters [9–11], fostering network entrainment via pacemaker neurons [2]. Theoretical and experimental research suggests that the neuron's ability to generate bursts of activity intrinsically arises from the expression of specific ion channels, such as hyperpolarization-activated inward transient potassium channels or calcium-dependent channels [2,12–14]. The kinetics of these channels form the basis of the slow dynamics.

Ion channels with dedicated slow kinetics, however, are not the only single-cell mechanism that can generate rhythms on long timescales. Specifically, an interplay between concentration dynamics and membrane dynamics has been shown to give rise to slow oscillations [15–17]. Here, we explore in detail how the combination of slower, pump-dependent extracellular potassium concentration dynamics with the faster spike generating dynamics can generate slow oscillations. We analyse the bifurcation structure in a minimalistic model, focussing on the role of the Na^+/K^+-ATPase. The minimalistic burst mechanism is based on a hysteresis loop arising from the feedback of the fast spiking dynamics to the slower concentration-dominated dynamics; the bistability arises in the fast subsystem [9,18,19]. We argue that via this mechanism, in principle, any class I nerve cell can be switched into an intrinsic burster even in the absence of channels with slow dynamics. For the proposed mechanism two facts are combined: (1) All neuron models that can produce arbitrarily slow firing rates (class I excitable neurons [20,21]) share the necessary fundamental bifurcation structure [19,22] and can be tuned into a bistable regime (where a stable fixed point and a limit-cycle co-exist) [23–25]. Alternating between the two stable states in the bistable regime is the basis of the deterministic bursting mechanism. (2) The electrogenic and concentration-dependent Na^+/K^+-pump can transform the fundamental bifurcation structure such that a hysteresis loop in a concentration

dimension can form under physiological conditions. The slow rhythm produced by this mechanism is expressed both at the level of neuronal spiking and ionic concentrations. It does require neither ion channels with slow dynamics nor rhythmic input via the neuronal network.

In the following, we first introduce a model exemplifying the proposed generic mechanism of slow deterministic bursting. Next, the mechanism is analysed by dissecting the slow and fast dynamics (here also termed the slow-fast method) [26]. Based on numerical continuation, the bifurcations in the fast subsystem are identified and the existence of a slow hysteresis loop mechanism is demonstrated. Finally, the conditions for which the model can be tuned into the slow bursting regime or other dynamics such as depolarization block and tonic spiking are discussed by analysis of the bifurcations in the complete system. Taken together, this study highlights the ubiquitous nature of the mechanism by which extracellular potassium dynamics and Na^+/K^+-ATPase can induce slow rhythms in single neurons and beyond.

Results

Modelling neurons in an extracellular environment

In order to study the emergence of slow rhythmic activity via the interactions of fast spiking and slow concentration dynamics (i.e., fast and slow subsystems, respectively. see next sections), a neuron model equipped with only basic fast spike-generating ion channels is placed in an external environment of fixed volume that contains extracellular potassium ions, whose concentration, $[K^+]_{out}$, can change (Fig 1). The interplay between concentration dynamics and neuronal voltage dynamics is modulated by the Na^+/K^+-ATPase in two-fold manner: First, the pump current directly affects the voltage dynamics. Second, the pump changes concentration gradients which, in turn, alter ionic reversal potentials. It will be shown in the subsequent section that this parsimonious setup suffices to create slow rhythms.

The neuron model, inspired by the Wang-Buzsáki model, comprises four currents: The depolarising Na^+-current and repolarising K^+-current are part of the spike-generating mechanism. A leak current balances the membrane potential in the rest state. For completing our model, we add a fourth current as a hyperpolarising pump current (I_p). This pump extrudes three Na^+ ions out of the cell while two K^+ ions are pumped in. The pump maintains the ionic gradient of the cell, which drives spiking activity. The activity of the pump is regulated by the extracellular potassium concentration, with higher $[K^+]_{out}$ resulting in increased pump strain (Eq 7). However, the pump's activity is limited by its maximum current capacity (I_{max}), which is influenced by both the electrophysiology characteristic of the pump and its density on the neuron's membrane. For the mathematical details, see Methods.

With each action potential, K^+ ions flow out of the cell through the voltage-dependent K^+ channels and accumulate in the extracellular space. The elevated extracellular potassium concentration ($[K^+]_{out}$), in turn, not only affects the pump current but also influences the neuron's excitability state via its effect on the reversal potential. Therefore, the dynamics undergoes a sequence of transitions, which form the basis for the rhythmic bursting behaviour and are explained and analysed in more detail in the following sections.

Pump- and extracellular potassium-mediated slow bursting

In this section, we first provide a brief illustrative description of the generic burst mechanism, leaving a detailed analysis of the conditions for its existence to the following sections.

An example trace of voltage and potassium concentration, respectively, for the slow bursting dynamics in a dedicated extracellular volume is depicted in Fig 2A. Each burst cycle contains two alternating states: quiescence and spiking. The rhythmicity of the voltage shows an

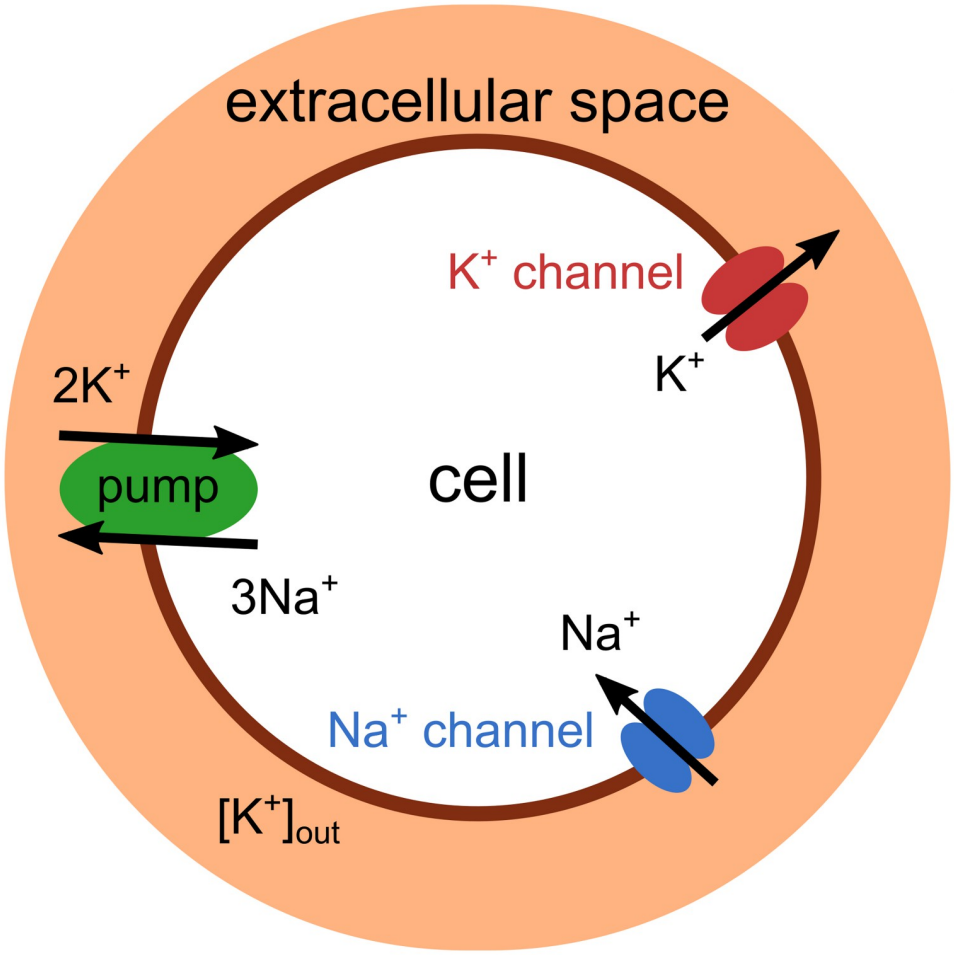

Fig 1. Schematic drawing of the neuron model in the extracellular environment. The concentration of extracellular potassium changes with the activity of voltage-gated potassium channels (red) and the Na^+/K^+-ATPase pump (green). The model equations governing the spike-generating inward sodium (blue) and outward potassium (red) currents correspond to those in the original Wang-Buzsáki model, retaining their fast dynamics. A slower timescale arises from the dynamics of the extracellular potassium concentration.

https://doi.org/10.1371/journal.pcbi.1011751.g001

inter-burst period of about one second. This period is about 30 times longer than the dynamics of one complete action potential in the spiking phase. The number of spikes per burst is fixed (i.e., bursting is deterministic).

The basic cycle undergone during a burst is summarised in Fig 2B. The burst relies on the bistable nature of the neuron's dynamics between spiking and quiescence. During the spiking period, the outward flow of potassium ions is considerable. The inter-spike interval does not provide sufficient time for the Na^+/K^+-ATPase to pump back all K^+ ions that left the cell during the spike. Consequently, K^+ ions accumulate in the extracellular space, resulting in a saw-tooth-like build-up of $[K^+]_{out}$ (Fig 2B, spiking phase). Furthermore, during the spiking phase of each burst, the inter-spike interval progressively prolongs as a result of K^+ accumulation in the extracellular space. Eventually, the rise of $[K^+]_{out}$ reaches a level where spiking is not possible anymore (the quiescent phase). Spiking is terminated by a homoclinic bifurcation (HOM) in the fast subsystem, indicated by the blue circle in Fig 2B. In the quiescent phase, the pump activity now suffices to reduce extracellular potassium, as the outward current via the potassium channels is significantly reduced in the absence of spike generation. Ultimately, the

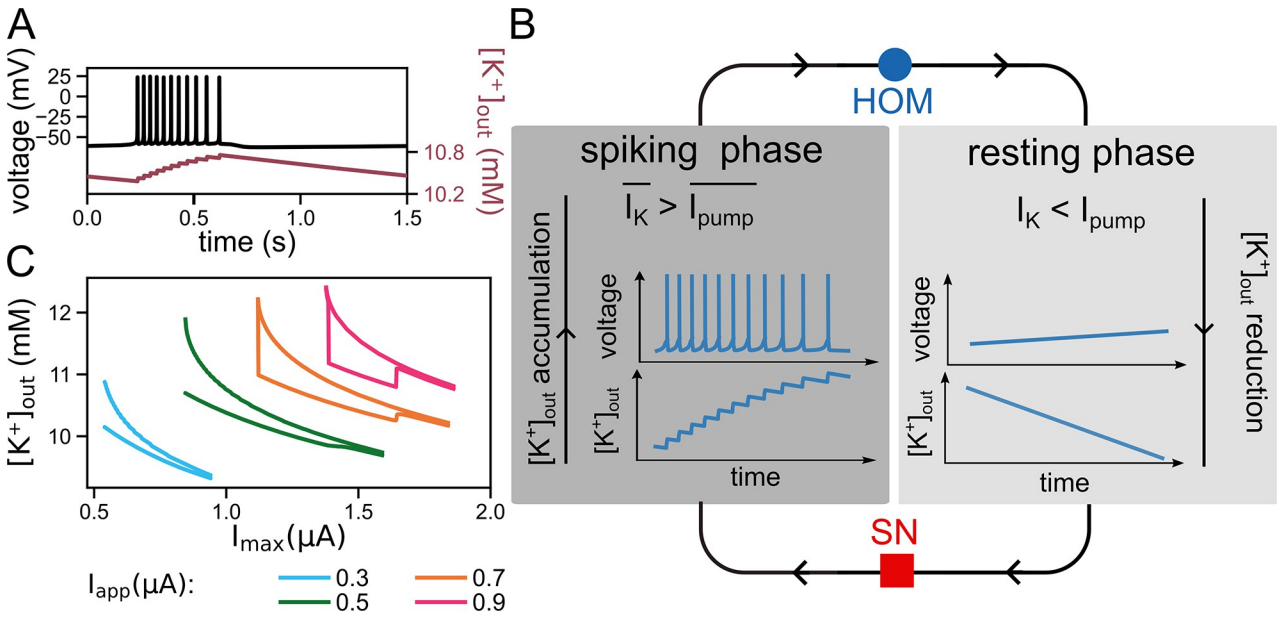

Fig 2. Bursting dynamics overview. (**A**) Each bursting cycle consists of two phases: a spiking phase and a quiescent phase, visible in the voltage trace. The concentration waxes with each spike and wanes during the quiescent phase. (I_{app} = 0.5 μA/cm^2, I_{max} = 1 μA/cm^2). (**B**) The spiking phase commences at a saddle-node (SN) bifurcation of the fast subsystem (red square). During the spiking phase, the average outward potassium flux through potassium channels surpasses the average inward potassium flux through the Na^+/K^+-ATPase leading to an accumulation of extracellular potassium. This phase terminates at a homoclinic (HOM) bifurcation of the fast subsystem (blue circle). From this bifurcation, the quiescent phase initiates, accompanied by a continuous decrease in extracellular potassium concentration due to the Na^+/K^+-ATPase current superseding the potassium current through the voltage-gated channels. This eventually results in a new spiking phase. (**C**) Minimal and maximal values of $[K^+]_{out}$ during an oscillation as a function of pump capacity (I_{max}) for different I_{app}. For each curve from right to left (decrease in pump capacity I_{max}): onset of bursting (inter-spike interval transitions from unimodal to bimodal), widening of the range of $[K^+]_{out}$ covered by the oscillations, finally burst termination (via depolarization block for I_{app} = 0.3 and 0.5 μA/cm^2, or initially double period and tonic spiking before entering depolarization block for I_{app} = 0.7 and 0.9 μA/cm^2).

https://doi.org/10.1371/journal.pcbi.1011751.g002

decrease of $[K^+]_{out}$, during quiescence results in another bifurcation of neuronal dynamics, corresponding to saddle-node bifurcation (SN) of the fast subsystem, see red square in Fig 2B. In passing this bifurcation, neuronal dynamics are back in the spiking region and the cycle starts all over again.

In Fig 2C, the amplitude of potassium concentration change is plotted as a function of the pump current density for different applied currents. At lower input currents, a decrease in pump density causes the potassium oscillation amplitude to grow. At high input currents, there is an additional jump-like increase in potassium oscillation amplitude that is caused by the chaotic dynamics of period doubling in the complete system bifurcation which is discussed in more detail below.

In summary, the spiking dynamics of the neuron impacts $[K^+]_{out}$, the latter of which, in turn, influences the K^+ reversal potential and hence the neuron's voltage dynamics. In the next sections, it will be shown that the identified mechanism is, indeed, a *hysteresis loop* where one branch of the bistable system corresponds to the spiking state and the other branches constitutes the quiescent state. The properties of the hysteresis loop are then further analysed in the slow-fast analysis section. The remainder of the article focuses on establishing how generic this mechanism is.

Slow-fast analysis

Neuronal bursting consists of an oscillation governed by two time scales: one corresponding to the fast spiking dynamics and one corresponding to the slower dynamics related to

concentration changes. Typically, these two different time scales result from either the presence of fast and slow currents [26], stochastic escape [27], external drive, synaptic delays [6], or as here, the slow variation of ions. All these cases benefit from a slow-fast analysis [26].

In the mechanism for the generation of slow rhythms proposed here, the fast subsystem is governed by the millisecond kinetics of the ion channels that shape the neuron's action potentials. In contrast, the slow subsystem is governed by the timescale of slow changes in $[K^+]_{out}$. The bursting rhythmicity of the system is thus regulated by an interplay between these two subsystems, which crucially depends on the activity of the Na^+/K^+-ATPase.

In slow-fast analysis, it is assumed that the timescale difference between the two subsystems is sufficiently large for them to be investigated separately. We will first subject the fast subsystem to bifurcation analysis while assuming that the slow subsystem undergoes only negligible variations on the timescales of the fast subsystem. Hence, $[K^+]_{out}$ can be treated as constant and the bifurcation parameter in this scenario. Subsequently, we will explore the dynamics of the slow subsystem assuming time-averaged values of the fast subsystem dynamics. More details on the method are to be found in the Methods section.

$[K^+]_{out}$ is a variable of interest featured in all figures related to slow-fast analysis. For consistency, it is depicted on the y-axis in all the figures addressing the dynamics of the system. To facilitate the comparison with other studies, the more conventional representation of the fast bifurcation diagram and slow dynamics (presenting bifurcation parameters on the x-axis) is given in S1 Fig.

Fast subsystem bifurcation analysis

For analysis of the fast, spike-generating subsystem, extracellular potassium concentration is approximated as a constant parameter. The bifurcation diagram in Fig 3 summarises the transitions in dynamics induced by changes in $[K^+]_{out}$.

Fig 3A shows a two-parameter bifurcation diagram of the fast subsystem spanned by the parameters extracellular potassium ($[K^+]_{out}$) and applied current (I_{app}) in the vicinity of the region used for the simulated traces in Fig 2A. Overlaid on the bifurcation diagram of Fig 3A are the dynamic changes of the complete system during a burst cycle with the parameters of Fig 2A shown as the black vertical line. If $[K^+]_{out}$ is low, the only stable state for the fast subsystem is a stable limit cycle (the dark grey area in both panels of Fig 3). In this region, the neuron spikes tonically. If $[K^+]_{out}$ is increased, the dynamics of the fast subsystem traverse the saddle-node (SN) bifurcation (the red line in Fig 3A). From the SN bifurcation, a saddle and a stable node emerge. When $[K^+]_{out}$ exceeds the SN bifurcation value, the neuron enters the bistable region (the white region in both panels of Fig 3). In the bistable region, the fast subsystem of the neuron model has two stable states, a stable limit cycle and a stable fixed point, separated by a separatrix originating from the stable manifold of the saddle. By raising $[K^+]_{out}$ even more, the blue line of a homoclinic orbit bifurcation (HOM) is crossed, at which the limit cycle of the action potential collides with the saddle and is annihilated. If $[K^+]_{out}$ passes this line, the fast system dynamics end up in the monostable zone, because at the HOM bifurcation, the stable limit cycle disappears. Hence, in the light grey part of Fig 3A, the neuron is in a quiescent state.

To better understand the bursting dynamics, the voltage trajectory of one burst cycle in the complete system (black solid line) is superimposed on the codimension-one ($[K^+]_{out}$) bifurcation diagram of the corresponding fast subsystem (coloured lines) in Fig 3B. The black trajectory depicts the burst dynamics presented in Fig 2A, however, instead of time the corresponding levels of $[K^+]_{out}$ are shown. The resulting phase portrait encompasses the complete system dynamics of the burst: In the dark grey region of Fig 3B the fast subsystem is in

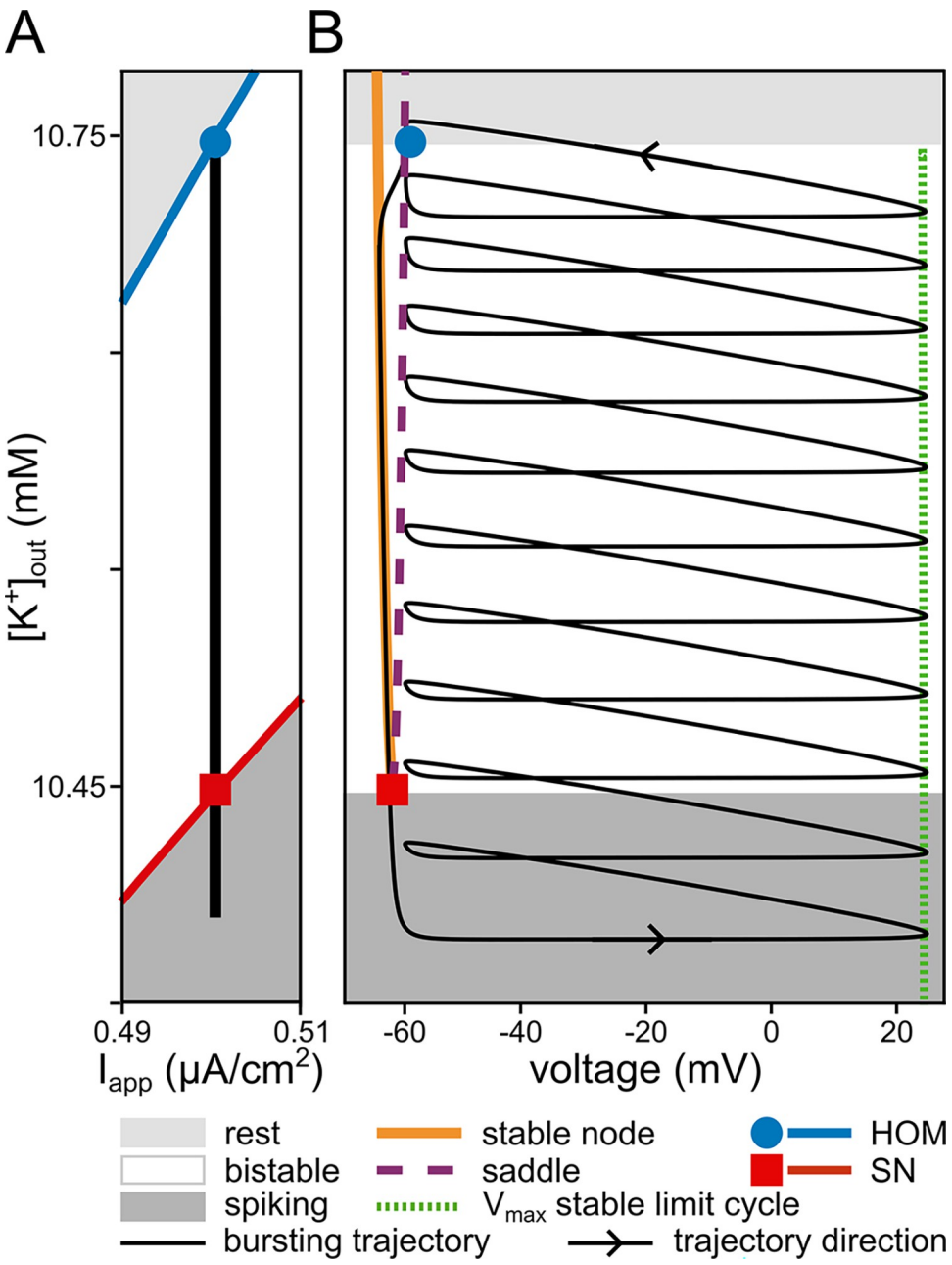

Fig 3. Bifurcations of the fast subsystem and bursting dynamics. The bistability of the fast subsystem is a requirement for the emergence of bursting dynamics in our system. (**A**) Two-parameter (extracellular potassium, $[K^+]_{out}$, and applied current, I_{app}) bifurcation diagram of the fast subsystem. The black vertical line indicates the range of $[K^+]_{out}$ values that the complete system traverses during the burst cycle shown in Fig 2A. The burst trajectory passes through the bistable region, bounded by the homoclinic (HOM) bifurcation at higher $[K^+]_{out}$ and the saddle-node (SN) bifurcation at lower $[K^+]_{out}$. During the spiking phase of the burst, $[K^+]_{out}$ builds up, whereas it depletes during the resting part. The black line extends into the tonic spiking domain of the fast subsystem due to the time spent near the ghost of the SN bifurcation. (**B**) Phase portrait of the complete burst (in voltage and $[K^+]_{out}$) onto the one parameter ($[K^+]_{out}$) bifurcation diagram of the fast subsystem. The black solid line demonstrates the same bursting dynamics as in Fig 2A.

https://doi.org/10.1371/journal.pcbi.1011751.g003

the tonic spiking mode. Here, the complete system (black trace) is going through a spiral path. Each rotation corresponds to one action potential. With each action potential, more K^+ accumulates in the extracellular space (see also Fig 2). By increasing $[K^+]_{out}$, the system enters the fast subsystem's bistable region (white area) and continues on the spiking branch. Note that if the neuron model was subjected to strong perturbations, jumps between the two attractors, a stable fixed point and a stable limit cycle, would occur. The effective increase in $[K^+]_{out}$ per spike diminishes as spiking progresses because the pump becomes more and more active due to the increase of extracellular potassium (Eq 7). Furthermore, the inter-spike interval increases because of the changes in the spiking dynamics caused by changes in the potassium reversal potential due to the accumulation of extracellular potassium.

Spiking continues until, eventually, $[K^+]_{out}$ reaches the HOM bifurcation (blue circle) and the stable limit cycle of the fast subsystem is annihilated. Here, the system enters the quiescent phase of the fast subsystem (light grey zone). In this phase, the only stable state is the rest state. Hence, the system trajectory leaves the spiking spiral and converges to the stable fixed point (orange line). In the rest state, $[K^+]_{out}$ is efficiently pumped back into the cell by the Na^+/K^+-ATPase (see also Fig 2). The pump activity increases the resting state voltage until an SN bifurcation is reached (red square). The saddle and the stable node collide and annihilate at this point. Thereby, the resting state loses stability and the system converges back onto the tonic spiking dynamics (dark grey), where the next burst cycle is initiated; for a zoom out of the bifurcation diagram in Fig 3B see S1 Fig.

Notable in both panels of Fig 3, there is a gap between the SN bifurcation and the onset of the first spike in a burst cycle. In this region, the voltage dynamics cannot, after passing the SN bifurcation, immediately jump to the spiking branch. The dynamics is slowed down by the proximity of the saddle-node bifurcation in the eigendirection associated with the eigenvalue that is still close to zero. This phenomenon is often referred to as ghost of the SN bifurcation (or, for brevity, the SN ghost in the rest of the article). Thus, the decrease of the $[K^+]_{out}$ does not immediately stop when the system reaches the SN bifurcation. $[K^+]_{out}$ is further reduced when moving away from the SN ghost until it can finally enter the spiking phase.

Slow subsystem analysis

The previous section analysed the spiking behaviour with the slow variable, specifically, the extracellular potassium concentration ($[K^+]_{out}$) treated as a parameter. The fast subsystem bifurcations that initiate and terminate spiking were identified. In this section, the dynamics of the slow subsystem is explored. The time scale of the slow subsystem is determined by the effect of spiking on $[K^+]_{out}$ in relation to the balancing effect of the Na^+/K^+-ATPase. Note that the effective pump rate depends on both the extracellular potassium concentration as well as the density of ATPase proteins (indirectly defined by I_{max}, see the Eq 7). Relevant quantities for the slow subsystem are thus the amount of K^+ leaving the cell per spike and the effective pump rates during the spiking and quiescent phases.

The slow concentration dynamics can be isolated by applying the method of averaging to the fast dynamics. It exploits the effect that the slow subsystem cannot track the rapid changes in the fast subsystem; effectively, it only senses the average impact of one complete spike. To calculate this average impact on the change of $[K^+]_{out}$, the pump current and the current carried by the fast spiking potassium channels are integrated over one spike period. The averaged quantity of the fast subsystem currents determines the time derivative of the slow subsystem and, consequently, its dynamics (see Eq 14). Note that when the fast subsystem is quiescent (i.e., no spiking), averaged and non-averaged fast subsystem dynamics are equal. With this averaging method, we can describe the dynamics of the slow subsystem as a reduced model

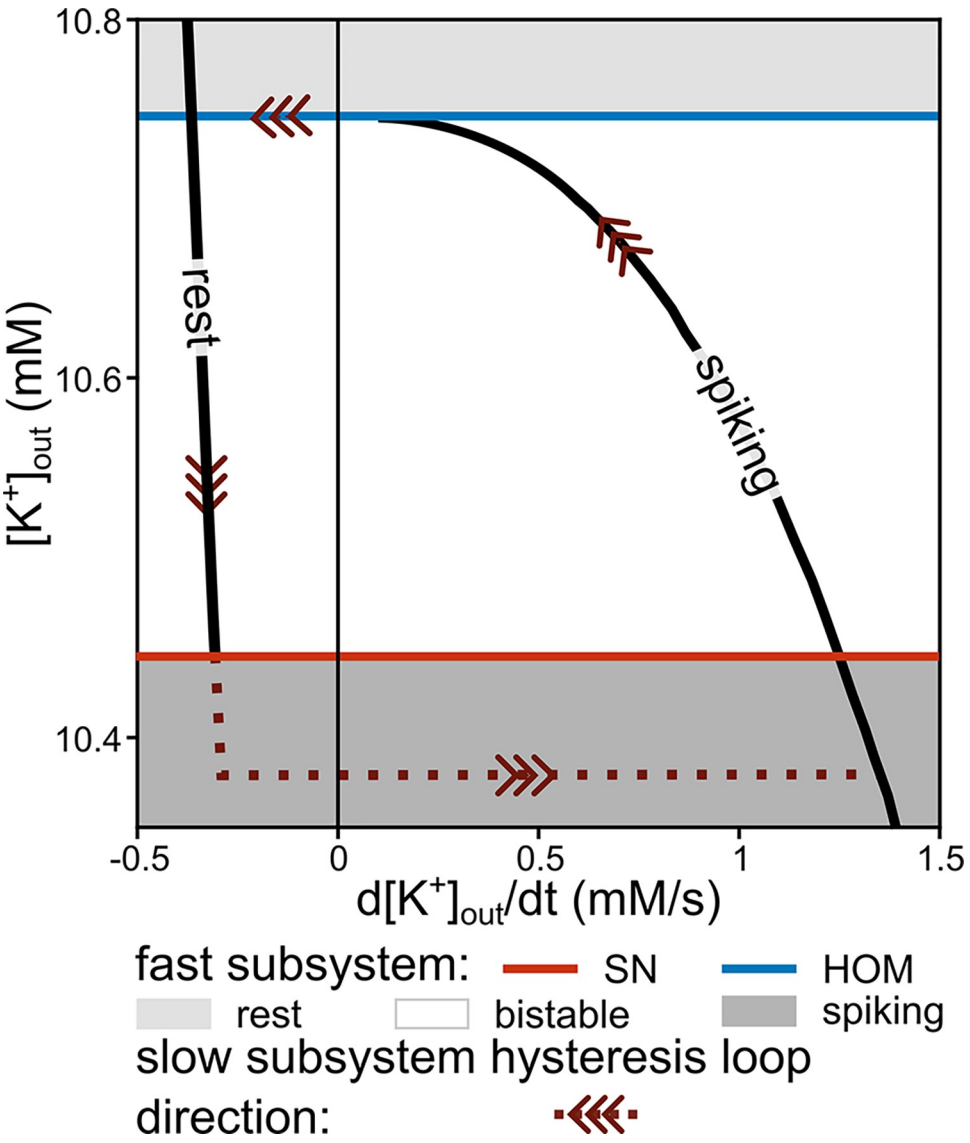

Fig 4. Hysteresis loop of the slow subsystem overlaid with the bifurcations of the fast subsystem. The extracellular potassium ($[K^+]_{out}$) dynamics of the reduced, slow subsystem entails a hysteresis loop oscillator. The slow oscillation organises around the bistable region of the fast subsystem, as also shown in Fig 3. The slow subsystem trajectory for the resting branch is calculated by inserting steady state fast variables as a function of the slow concentration into the $[K^+]_{out}$ time derivative (see Methods, Eq 9), while the spiking branch requires averaging (see Methods, Slow-fast method, Eq 14). The red and blue lines represent the location of the saddle-node (SN) and homoclinic (HOM) bifurcations of the fast subsystem according to ($[K^+]_{out}$), respectively. Note that, after going through the SN bifurcation, the system remains near the SN ghost for a while before spiking is resumed (brown dotted line). Parameters as in Fig 2A.

https://doi.org/10.1371/journal.pcbi.1011751.g004

that can capture the complete system dynamics. See Methods for more details on the averaging method and [26] for an introduction.

Fig 4 shows the phase portrait of the reduced slow subsystem, in terms of $[K^+]_{out}$ and its temporal derivative, for the specific parameters used in Fig 2. In analogy to Fig 3, in Fig 4 areas of tonic spiking (dark grey), bistability (white), and quiescence (light grey) of the fast subsystem are marked. The HOM and SN bifurcations of the fast subsystem mark the borders of these zones, (blue and red horizontal lines). Trajectories of the reduced slow subsystem

corresponding to spiking and quiescence of the fast subsystem are indicated by the labels 'spiking' and 'rest', respectively.

Fig 4 reveals the hysteresis nature of the slow subsystem (reduced system), which revolves around the bistability of the fast subsystem. The bistability of the fast subsystem serves as the prerequisite for the existence of the hysteresis loop in the reduced slow subsystem. For clarification of the mechanism, we follow the $[K^+]_{out}$ hysteresis loop in Fig 4 through the same sequence of bifurcations as in Fig 3B. If our fast subsystem is spiking (equivalent to the spiral path in Fig 3B), this corresponds to the spiking branch of the hysteresis loop in Fig 4 and the time derivative of $[K^+]_{out}$ is positive. This means that in each cycle of an action potential, the mean K^+ flux into the extracellular space is larger than the mean of the K^+ flux via the pump, which reabsorbs potassium ions into the neuron. In other words, extracellular K^+ accumulates continuously in extracellular space. However, while the slow subsystem slides up on this branch (from right to left) through the bistable region, the potassium increment reduces with every additional spike. With the parameters used here, the spiking branch of the slow subsystem terminates at the HOM bifurcation before the derivative of $[K^+]_{out}$ turns negative. This observation depends on the system's parameters, as it is further explored below. After the HOM bifurcation of the fast subsystem, the slow subsystem falls back to the stable resting branch.

In the quiescent state of the fast subsystem (light grey region), the K^+ flux via the Na^+/K^+-ATPase dominates, as there is no spiking and, consequently, no major flux of potassium out of the neuron. Therefore, the time derivative of $[K^+]_{out}$ is negative (Fig 4, rest branch). $[K^+]_{out}$ decreases and potassium is pumped back into the neuron. The slow subsystem follows the quiescence branch from higher to lower $[K^+]_{out}$ through the bistable zone (equivalent to sliding on the orange line in Fig 3B). At the SN bifurcation (red line), the stable node disappears from the fast subsystem's dynamics. As a consequence, the silent branch comes to an end at a lower $[K^+]_{out}$. Subsequently, the reduced slow subsystem undergoes a transition to the spiking branch after passing through the ghost of the SN bifurcation. This completes the hysteresis loop of the reduced slow subsystem.

In summary, the bursting process is enabled by the bistability of the fast subsystem and corresponds to a hysteresis loop. The bistability allows the system to alternate between quiescence (where the activity of the Na^+/K^+-ATPase suffices to extrude potassium from the extracellular space) and spiking (marked by accumulation of potassium in the extracellular space).

Generic occurrence of the burst mechanism

The previous sections described how, for specific parameter settings, class I conductance-based neuron models can exhibit slow bursting when the dynamics include the activity-dependent concentration changes in an extracellular space of fixed volume. The following section investigates the robustness and prevalence of the described burst mechanism and its dependence on model parameters.

The pump's essential contribution to the bursting mechanism. To investigate the influence of the electrogenic Na^+/K^+-ATPase, we switched off the pump current in the model's voltage equation, yielding a system similar to [15] (see Fig 5A, and compare it to the full model with an electrogenic pump current Fig 5B). At higher input currents, the Na^+/K^+-ATPase switches the system from turning towards the depolarization block in all cases to a system that can transition from rest via tonic firing to proper bursting and only then depolarization block. The electrogenic pump activity shifts the depolarization block to higher inputs.

As the mechanism of bursting relies on a region of bistability in the fast subsystem, one may note that the generic unfolding of a codimension-two saddle-node loop (SNL) bifurcation

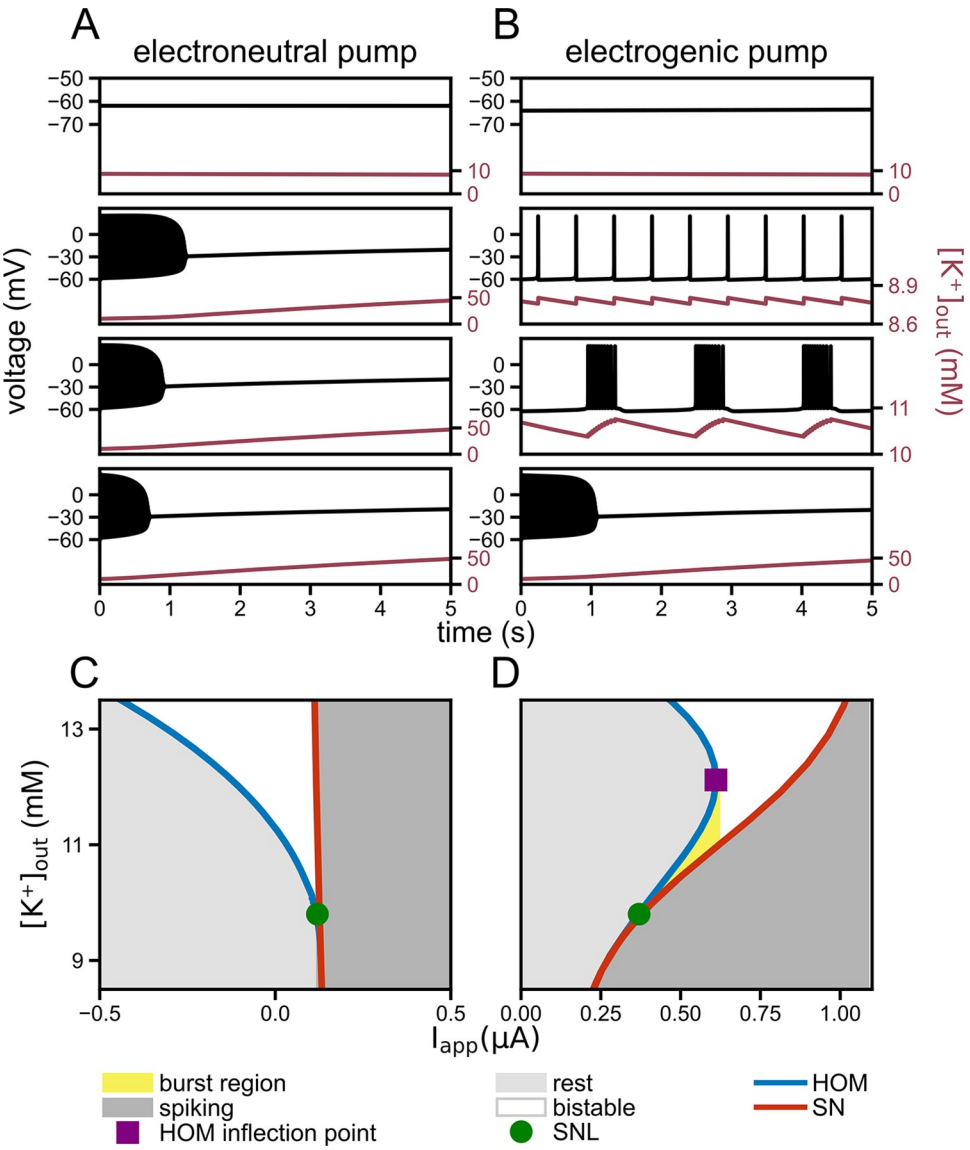

Fig 5. Shear transformation of the saddle-node loop (SNL) unfolding induced by the Na^+/K^+-ATPase. Including a Na^+/K^+-ATPase into the neuron model affects the fast subsystem bifurcation diagram and thereby enables bursting dynamics in the complete system. (**A**) and (**B**): Voltage traces from the models with an electroneutral (akin to [15]) and with an electrogenic Na^+/K^+-ATPase for different values of the applied current I_{app} (0.1, 0.25, 0.5, 0.9 μA/cm^2, top to bottom). Tonic spiking and bursting dynamics occur in the paradigm with pump. (**C**) Two-dimensional bifurcation diagram of the fast subsystem with the electroneutral pump. The generic unfolding of the SNL bifurcation (green circle) includes a bistable area between the homoclinic (HOM) and saddle-node (SN) bifurcation lines. (**D**) In the model with electrogenic pump, the area of bistability is sheared. This opens up the possibility for a $[K^+]_{out}$ hysteresis loop (yellow region) for values of I_{app} between the SNL (green circle) and the HOM inflection point (purple square). I_{max} = 1 μA/cm^2 in all panels.

https://doi.org/10.1371/journal.pcbi.1011751.g005

[28] from the neuron model with an electroneutral pump includes a region of bistability (Fig 5C) [29]. For the burst mechanism to work, however, the fast dynamics along the $[K^+]_{out}$ direction (with constant I_{app} in Fig 5C) needs to be bounded by HOM and SN branches for higher and lower values of $[K^+]_{out}$, respectively (compare Figs 5C and 3A). This is possible, if the bifurcation diagram is sheared such that the HOM and SN branches bend to the right. Interestingly, such shearing occurs as a result of adding a K^+-dependent electrogenic pump

(Eq 7) to the neuron model with an SNL bifurcation (see Fig 5D). The pump current acts as an applied current that depends on $[K^+]_{out}$; in our model it is a sigmoidal function with half activation at 11 mM. The pump induces a shear transformation of the canonical unfolding of the SNL bifurcation (Fig 5D). The larger the maximum pump current (I_{max}), the larger the shear. The Na^+/K^+-ATPase density in the membrane (directly related to I_{max}), hence is a crucial parameter for the emergence of bursting by the minimalistic mechanism proposed here.

The region of burst occurrence in the fast subsystem (yellow area in Fig 5D) is bounded by the SNL point (green circle) and the inflection on the HOM branch (purple square). For I_{app} beyond the inflection point, spiking continues until $[K^+]_{out}$ reaches a fold of limit cycles (FLC), which is analysed in the next section.

In summary, the burst mechanism relies on two essential ingredients from the neuron's fast subsystem, which enable the hysteresis loop:

1. For low $[K^+]_{out}$, the onset of spiking in the fast subsystem occurs via a saddle-node on invariant cycle (SNIC) bifurcation (typically present in neurons with class I excitability). This implies that the neuron model also undergoes an SNL bifurcation; at higher $[K^+]_{out}$ [22,25], opening up the bistable region between a homoclinic and a SNIC branch (Fig 5C).
2. The electrogenic Na^+/K^+-ATPase counteracts the K^+ efflux and mediates the coupling between $[K^+]_{out}$ and neuronal voltage dynamics. The pump's activity shears the bistable region such that it can be traversed by changes in $[K^+]_{out}$ while being bounded by a fixed-point region (quiescence) from above and a limit-cycle region (tonic spiking) from below (Fig 5D).

Dynamics in the proximity of the bursting region. To comprehensively understand the model's dynamics, we need to take a detailed look at the dynamics occurring in the vicinity of the bursting in the full system to shed light on factors that constrain bursts, the dependence on parameters, and the robustness of the described mechanism.

Zooming further out of the K_{out}-I_{app} plane depicted in Fig 3A reveals additional structures in which the region of bistability of the fast subsystem is embedded (Fig 6A). The vertical trajectories overlaid on the fast subsystem bifurcation show the direction of the slow subsystem (i.e., complete system) dynamics. According to Fig 6A, variation of the applied current resulted in different dynamics of the complete system. The slow bursting is possible in the range of I_{app} between SNL (green circle) and the HOM inflection point (purple square), as is the case in the yellow area in Fig 5D. The specific bursting dynamics of Fig 2A is found in the parameter region D in Fig 6A.

For I_{app} higher than the HOM inflection point (purple square in Fig 6A), the complete system dynamics ends up in depolarization block. After passing through a Hopf bifurcation, the neuron loses the ability to spike in a fold of limit cycles (FLC) bifurcation. This can be referred to as a depolarization block. The letter B in Fig 6A corresponds to one example that converges towards depolarization block. If the system starts in low $[K^+]_{out}$ at position B, i.e., the tonic spiking region of the fast subsystem (dark grey area), with each spike, $[K^+]_{out}$ increases, moving the system upwards along the flow field direction of the complete system (filled black arrows in Fig 6A). The system passes the bistable zone but does not encounter the HOM bifurcation. The limit cycle terminates in an FLC bifurcation instead. The same can also be seen in the dynamics of the reduced slow subsystem for the same modelling parameters (Fig 6B). Here, if we start from the spiking branch (solid line), the time derivative of $[K^+]_{out}$ is positive. Hence, the system slides on the spiking branch from lower to higher $[K^+]_{out}$, until it reaches the FLC bifurcation. At this point, the spiking branch terminates, and the system jumps to the

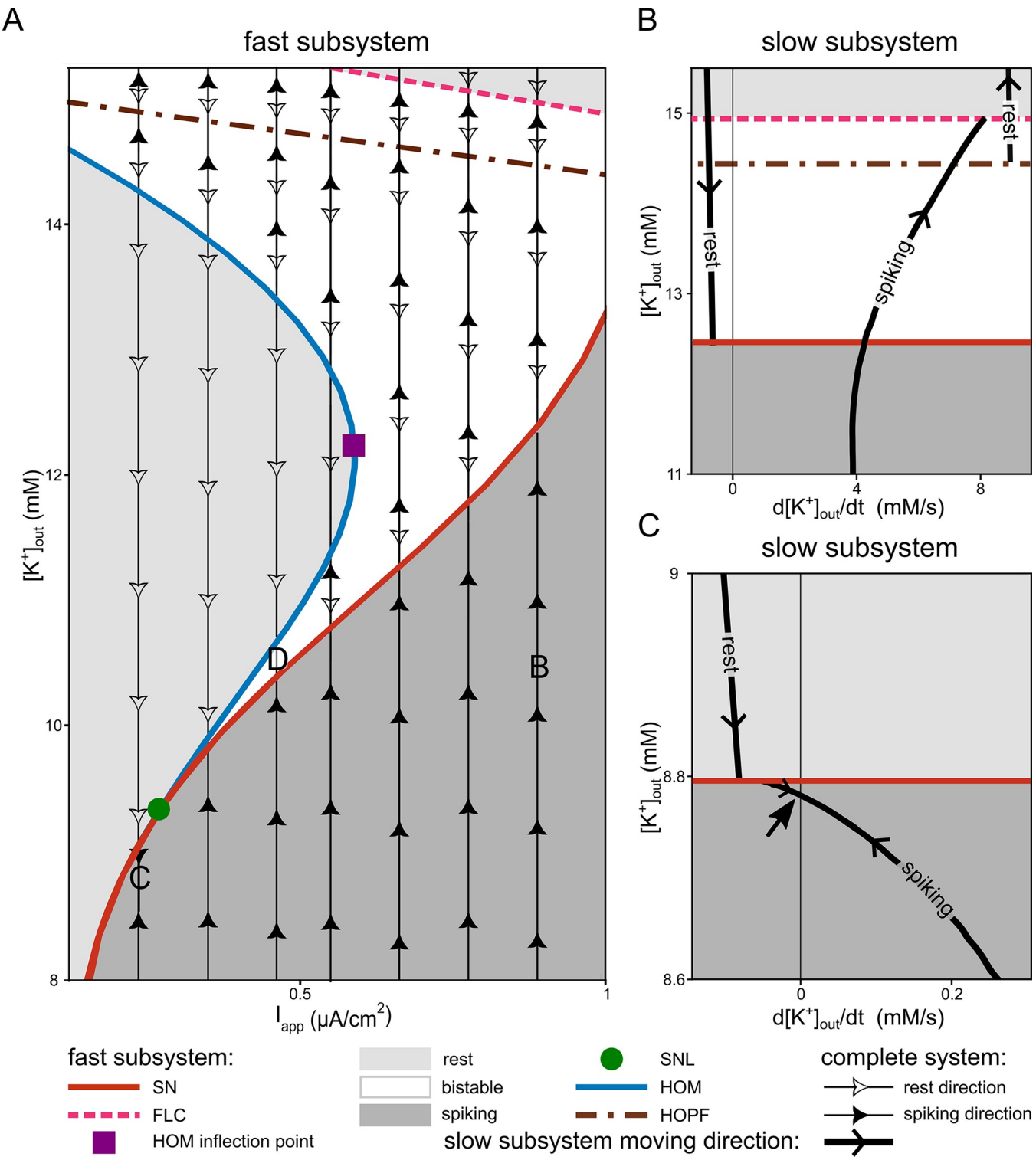

Fig 6. Bifurcations of the fast subsystem with an overlaid phase portrait around the bursting region. The bifurcations of the fast subsystem together with the flow of dynamics is shown in the vicinity of bursting area. (**A**) Zoom-out of the two-parameter bifurcation diagram of the fast subsystem depicted in Fig 3A. Depending on the applied current (I_{app}) and extracellular potassium concentration ($[K^+]_{out}$), the fast subsystem exhibits mono-, bi-, or even multistability. The resting region in the top right corner, above the fold of limit cycles (FLC) is characterised by bistability between two fixed points. The region between the Hopf and FLC bifurcations is multistable between two fixed points and one limit cycle. The bistable region enclosed between the homoclinic (HOM), saddle-node (SN), and Hopf bifurcations enables bursting. Here, the bistability occurs between one limit cycle and one fixed point. The burst is possible for values of I_{app} between the ones corresponding to the saddle-node-loop (SNL) and HOM inflection point. The area marked as D highlights where the bursting shown in Fig

2A occurs. The vertical arrows indicate the flow field direction of the complete system. For the higher $[K^+]_{out}$ than the Hopf line, the one branch of the complete system flow field direction which is going to higher $[K^+]_{out}$ and indicating the depolarization block branch is not shown (see panel B, rest branch with positive time derivative of $[K^+]_{out}$). Two specific cases are selected from the region of depolarization block (B) and tonic spiking (C) of the complete system dynamics for further study. (**B**) Reduced slow subsystem dynamics overlaid on the bifurcation of the fast subsystem in the case marked as B in panel A (I_{app} = 0.9 μA/cm^2). This case corresponds to a transition to the depolarization block in the complete system. The arrangement of the resting and spiking branches indicates that, regardless of where the system starts on this diagram, it will eventually reach the resting branch with the higher time derivative of $[K^+]_{out}$ and follow that line up to the depolarization block. (**C**) Reduced slow subsystem dynamics overlaying on the bifurcation map of the fast subsystem in the case marked as C in panel A (I_{app} = 0.25 μA/cm^2). This case corresponds to tonic firing in the complete system. The black straight vertical line represents $d[K^+]_{out}/dt = 0$, and the arrow indicates the spiking branch of the slow subsystem crossing this line and having a stable fixed point. Accordingly, the complete system remains tonically firing. I_{max} = 1μA/cm^2 for all the panels.

https://doi.org/10.1371/journal.pcbi.1011751.g006

resting branch with a positive time derivative of $[K^+]_{out}$ instead of the normal resting state. The time derivative of $[K^+]_{out}$ on this branch is positive because this state corresponds to an upstate voltage at which more voltage-gated channels are in a conducting state. With the given I_{max}, the pump is insufficient to compensate and $[K^+]_{out}$ continues to increase until the silent branch eventually approaches zero in a very large $[K^+]_{out}$. If the system starts at $[K^+]_{out}$ higher than the SN bifurcation of the fast subsystem and is on the other resting branch of the slow subsystem (left side of the Fig 6B), however, the negative time derivative moves the system along this branch in the direction of decreasing $[K^+]_{out}$. As it progresses, the system reaches the SN bifurcation, transitioning into a spiking state, and eventually leading to the depolarization block.

At I_{app} below the SNL bifurcation in Fig 6A, tonic spiking is possible. An example from the tonic spiking area is indicated by the letter C in Fig 6A. The bistable region, which is a requirement for the bursting mechanism under investigation, is absent in the fast subsystem bifurcation for this case. As shown in Fig 6A, in the vicinity of the position marked C, two dynamical regimes for the fast subsystem exist: tonic spiking and quiescence. Why has the complete system a stable state at tonic spiking? The answer can be read of Fig 6C, which depicts the time derivative of the reduced slow subsystem. The spiking branch of the reduced slow subsystem crosses zero with a negative slope (see arrow in Fig 6C); the reduced system has a stable fixed point. This fixed point is in the region where the only attractor in the fast subsystem is a stable limit cycle. The silent branch in Fig 6C is lower than zero. Consequently, if we start on this branch, the reduced slow subsystem eventually jumps to the spiking branch and reaches the stable fixed point. Thus, the complete system in the region around C ends up in the spiking regime.

Note that, in Fig 6A, for I_{app} lower than the HOM inflection point of the fast subsystem and $[K^+]_{out}$ higher than HOM bifurcation in the bistable region of the fast subsystem, the complete system dynamics are similar to the dynamics of Fig 6B, where $[K^+]_{out}$ is higher than the fast subsystem SN bifurcation. Therefore, two directions for the complete system dynamics exist. The first one increases $[K^+]_{out}$, resulting in depolarization block. The second one decreases $[K^+]_{out}$, in contrast to the scenario in Fig 6B, resulting in either tonic spiking or bursting, in dependence of the size of I_{app}. Hence, the dynamics of the complete system exhibits bistability (depolarization block versus either bursting or tonic spiking).

In this section, we demonstrated that our basic neuron model possesses the ability to not only generate slow rhythmic bursting activity but also to exhibit other significant dynamics such as tonic spiking and depolarization block. Each of these dynamics plays a crucial role in both physiological and pathological scenarios.

Dependence of the bursting mechanism and other dynamics on the pump density. We saw that Na^+/K^+-ATPases are crucial for the feedback from the fast to the slow dynamics. The pump density, denoted in our model by I_{max}, is thus a natural parameter to investigate the robustness of the described bursting mechanism, regarding both the existence and extent of a

bursting region. In Fig 7A, the complete system dynamics is explored in the I_{max}-I_{app} plane. Four regions are identified, each associated with a distinct regime of the complete system: rest, tonic spiking, bursting, and depolarization block. As a reminder: In the previous sections we examined representative cases from the bursting (Figs 2–4 and label D in Fig 6A), depolarization block (label B in Fig 6A and 6B), and tonic spiking (label C in Fig 6A and 6C) regions, all of which shared the same I_{max} value (1 μA/cm2). In contrast, here I_{max} is varied.

First, we can see in Fig 7A that the larger the pump density, the larger the applied current needs to be to achieve depolarization block. For completeness, note that, as mentioned in the analysis of Fig 6, in the regions labelled as rest, tonic spiking and bursting, the complete system can also directly converge to depolarization block when the initial potassium concentration is large, depending on the other initial conditions. In contrast, in the region labelled as depolarization block, i.e., for I_{app} beyond the HOM inflection point of the fast subsystem (purple dotted curve), the depolarization block will inevitably be reached, even starting from low $[K^+]_{out}$. Numerical continuation of the complete system shows that the limit cycle corresponding to tonic firing disappears in a fold of limit cycle bifurcation (pink curve in Fig 7A; pink star in Fig 7D). Beyond this bifurcation, only the large-$[K^+]_{out}$ stable branch of fixed points remains (orange solid curve in Fig 7D), leaving depolarization block as the only possible outcome.

We now examine the bursting region. In the preceding sections, we established the essential role of the pump current in opening up a range of applied current values for which bursting can potentially take place: for a constant I_{app} between the fast subsystem SNL bifurcation and HOM inflection point, the fast subsystem possesses a region of bistability, bounded by the homoclinic and saddle-node bifurcations (Fig 5D). This configuration is a necessary condition for the formation of the hysteresis loop that drives the bursting dynamics. The bursting region (yellow area in Fig 7A) is therefore constrained by the SNL bifurcation and HOM inflection lines of the fast subsystem (depicted in dotted green and purple lines, respectively). The bursting region initially expands with Imax as these two lines diverge, until at some point, although the requirement for bursting is still met, it shrinks and terminates. In the remaining area between the two lines, the complete system exhibits tonic spiking instead of bursting.

We conducted a case study in this particular zone, at the point in parameter space position marked E in Fig 7A. The corresponding slow-fast analysis diagrams are shown in Fig 7B and 7C. The fast subsystem does indeed fulfil the essential prerequisites for bursting: bistability between quiescence and tonic spiking for potassium concentrations comprised between the homoclinic and saddle-node bifurcations (Fig 7B). However, the reduced slow subsystem features a stable fixed point inside this region of bistability, marked with an arrow in Fig 7C. It corresponds to a stable limit cycle of the complete system, during which the contributions of the pump and voltage-gated channels to potassium dynamics cancel each other out on average. In this situation, in contrast to the case studied in Fig 3–4, the hysteresis loop fails to form and the complete system stabilizes in a tonic firing state (position E in Fig 7B) instead of bursting.

When approaching the bursting region from the tonic spiking region, the stable fixed point of the reduced slow subsystem moves progressively closer to the homoclinic bifurcation of the fast subsystem. Near the bifurcation points of the fast subsystem, the slow-fast method and analysis of the reduced slow subsystem fails because the timescale of the fast subsystem increases to the point the separation of the fast and slow timescale is not possible anymore. To better understand the transition between tonic spiking and bursting, we performed a numerical continuation of the complete system. We find that the limit cycle corresponding to tonic spiking destabilizes in a supercritical period doubling cascade to become the bursting solution (light blue curve in Fig 7A, light blue dots in Fig 7D). An in-depth investigation of the transfer to the bursting state in this region as well as of mechanisms that add extra spikes during bursting (also termed spike-adding mechanisms [30]) is beyond the scope of this work. We can,

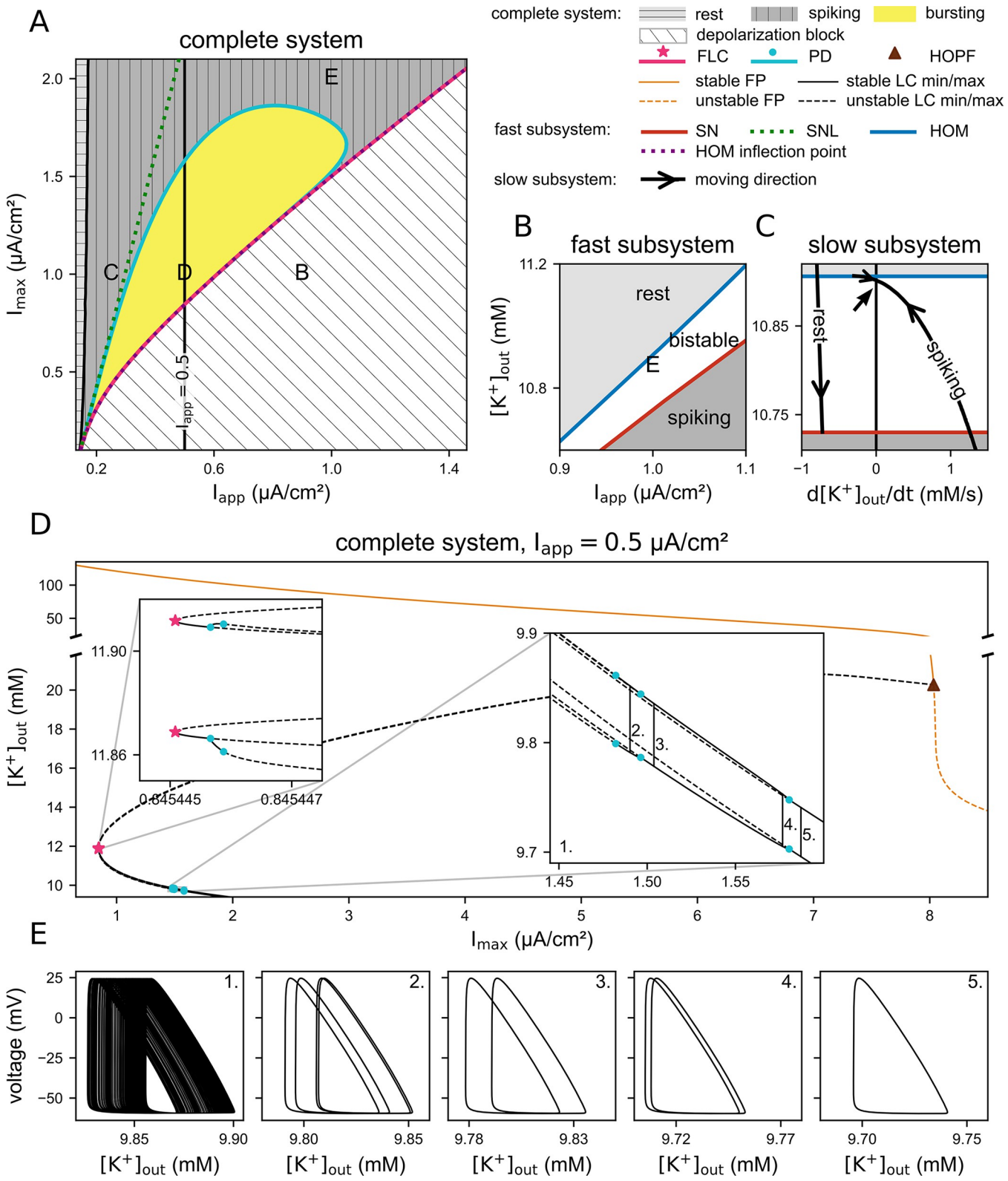

Fig 7. Dynamics of the complete system for varying pump density. Depending on the maximal pump current (I_{max}) and applied current (I_{app}), the complete system can show different dynamics (rest, tonic spiking, bursting, and depolarization block). This figure focuses on a low potassium concentration. (A) Bifurcations in the complete system as well as the corresponding fast subsystem saddle-node-loop (SNL) and HOM inflection point. The points labelled B, C, and D in this figure correspond to the same parameter sets as shown in Fig 6 with the same labelling. The area between the saddle-node-loop (SNL) and HOM

inflection point lines of the fast subsystem represents the parameter space where bursting can potentially occur, according to the fast subsystem analysis. Within this region, the complete system displays bursting behaviour only in the yellow zone. Numerically, the boundary of the bursting region is verified by detecting the transition of the interspike interval distribution from unimodal (tonic spiking) to bimodal (bursting). This boundary aligns with the period-doubling (PD) bifurcation line of the complete system. (B) Two-parameter (extracellular potassium $[K^+]_{out}$, and I_{app}) fast subsystem bifurcation diagram for the case indicated by E in panel A (I_{max} = 2 μA/cm^2, I_{app} = 1 μA/cm^2). The necessary condition for bursting, i.e., a bistable region bounded by homoclinic (HOM) and saddle-node (SN) bifurcations from above and below, respectively, is satisfied. (C) Reduced slow subsystem dynamics overlaid onto the bifurcation map of the fast subsystem corresponding to letter E in panels A and B. The spiking branch of the reduced slow subsystem intersects the line $d[K^+]_{out}/dt = 0$, indicated by the black arrow. This intersection signifies the presence, on the spiking branch, of a stable fixed point of the reduced slow subsystem, within the bistable region of the fast subsystem. Consequently, the complete system exhibits tonic spiking, despite the fast subsystem meeting the conditions for bursting (D) One-parameter bifurcation diagram ([K+]out, Imax) of the complete system; Iapp = 0.5 μA/cm2. Insets: zoom in near the borders of the bursting region, where the complete system undergoes cascades of supercritical period doubling bifurcations. Note that this bifurcation diagram is not exhaustive. (E) Consecutive samples along the period-doubling cascade shown in the inset on the right-hand side of panel D. E_5 to E_2: stable limit cycles before the first PD (case 5: I_app = 1.5897 μA/cm2), between the first and second PD (cases 4 and 3: I_app = 1.5767, and 1.5037 μA/cm2, respectively) and between the second and third PD (case 4: I_app = 1.4903 μA/cm2). E_1: chaotic trajectory further down the cascade (I_app = 1.45 μA/cm2), obtained by direct simulation for 90 seconds.

https://doi.org/10.1371/journal.pcbi.1011751.g007

however, predict that it involves both chaos-induced (see period-doubling route to chaos in Fig 7D and 7E) and canard-induced (see jump-on canard solution in S2 Fig) mechanisms, similarly to what was reported for the phenomenological Hindmarsh-Rose neuron model, for example in [31]. Such phenomena are commonly found in Fold/HOM bursters and have been thoroughly analysed in several models of excitable cells [32–37]. Period doubling has previously been shown to be inducible by changes in the extracellular bath concentration [16].

From this section, it becomes clear that the Na^+/K^+-ATPase plays a pivotal role in various dynamics possible in models with class I spike generating dynamics, when extracellular potassium dynamics are taken into account. A higher pump density contributes to postponing the depolarization block. Moreover, while the pump can establish the necessary conditions for bursting, a pump current that is too strong can also suppress bursting incidents.

Finally, we briefly note that the mechanism was also tested in the presence of dynamic Na^+ concentrations. To this end, we modified the model by incorporating intracellular sodium concentration ($[Na^+]_{in}$) dynamics through Eqs 11 and 12 and by adjusting the Na^+/K^+-ATPase equation to also account for changes in $[Na^+]_{in}$ (see Eq 13). The result is shown in S3 Fig. The desired bursting mechanism is present in the modified model, too. However, including $[Na^+]_{in}$ dynamics in the model can introduce more intricate behaviours. For example, in of S3A Fig, sodium slightly accumulates over time and can result in alterations of spike amplitude and spiking threshold [38]. These dynamics, however, are not the focus of this paper.

Discussion

In this article, we demonstrate that a neuron whose dynamics of extracellular potassium are taken into account requires only two essential elements to exhibit slow bursting: a bistable region arising from an SNL bifurcation and a feedback loop mediated by a Na^+/K^+-ATPase. In contrast to some previous models for slow bursting, this firing mode requires neither ion channels with slow dynamics nor rhythmic inputs. Our slow-fast bifurcation analysis reveals a ubiquitous mechanism: square-wave bursting via a fold-homoclinic hysteresis loop, requiring only a single slow concentration variable. This mechanism, in principle, can be encountered in all class I excitable neurons with spike onset via a SNIC bifurcation, the spiking dynamics of which have been shown to be tuneable into an SNL regime via a number of physiological parameters [22,25]. The evidence presented assigns a pivotal role to the Na^+/K^+-ATPase in the generation of slow bursting, tonic spiking, and depolarization block. The exploration of the mechanistic core and robustness of the described bursting mechanism provides novel perspectives on elevated extracellular potassium levels in neural pathologies such as seizures or spreading depolarization and potentially their treatment.

The relevance of the Na^+/K^+-ATPase

Our findings highlight the large influence of Na^+/K^+-ATPases [39,40] on the dynamics of neuronal spiking. Different isoforms of the pump are known as generic players in the homeostasis of extracellular potassium, the resting potential, as well as cell volume. Previous experimental evidence already indicated that neuronal Na^+/K^+-ATPase function extends beyond the stabilization of extracellular potassium. Along these lines, it has been argued that if most of the potassium secreted by neurons was siphoned off by astrocytes, neuronal activity could not continue for tens of seconds because of imbalances in potassium concentration [41]. Our model indicates yet another function of the Na^+/K^+-ATPase: as an enabler of rhythmic activity when extracellular potassium concentration is elevated. While previous studies assigned a mechanistic role to the Na^+/K^+-ATPase for rhythmic bursting in pattern generators [42,43], it was the interaction between h-currents and the pump for control of Na^+ that was emphasized; the burst mechanism proposed in this paper was not investigated. The involvement of the Na^+/K^+-ATPase in the induction of rhythmic activity is consistent with a previous proposal [44]. Kager and colleagues indicated that $[K^+]_{out}$ or voltage-dependent ion channels that elicit inward currents can generate seizure-like rhythmic activity, provided that the inward current secondarily triggers the release of K^+ into a confined extracellular space–a set of conditions met by the Na^+/K^+-ATPase.

Our model predictions match a number of observations in pathological states. For example, our results that a higher pump density shifts the initiation of the bursting mode and depolarization block towards higher input currents agree with the experimental observation that the Na^+/K^+-ATPase helps to inhibit seizures and SD. Specifically, inactivation of the neuron-specific alpha3-isoform of Na^+/K^+-ATPase has been shown to induce seizures in mice [45]. Further, the loss-of-function mutation that causes chorea-acanthocytosis is accompanied by an impaired capacity of the Na^+/K^+-ATPase in neurons, and epilepsy is among the symptoms of this neurodegenerative disorder [46], potentially fostered by the bursting mechanism at hand. Even partial inactivation of the Na^+/K^+-ATPase with ouabain has been shown to cause SD-like depolarization: An epileptic population spike is followed by an ouabain-induced SD [47], which is consistent with the cellular dynamics observed in the model presented here. Moreover, a shortage of oxygen or ATP as it may, for example, occur during ischemia, renders the pump less effective. We demonstrate that an insufficient pump current can first induce bursting and then facilitate depolarization block. This agrees with depolarization events occurring in hypoxic and ischemic conditions [47,48] as well as previous suggestions that hypoxia or an impaired pump can move neurons into seizure states [44,49]. In addition, an experimental study has revealed a correlation between seizures and lowered oxygen pressure levels. Decreases in oxygen pressure can first induce seizures but also stop them at even more oxygen-deprived levels [50]. Our model, in alignment with these experimental findings, indicates that–although an insufficient pump current can trigger seizures (i.e., bursting)–a too strong reduction in pump activity can again terminate bursting (and thus potentially seizures) because the pump's activity positively correlates with oxygen levels [49].

The Na^+/K^+-ATPase density sets four dynamical regimes

The present biophysical model also demonstrates the ability to exhibit both bursting and depolarization block, which aligns with previous observations indicating that seizures and spreading depolarizations (SD) can originate from the same neuronal population [51,52]. Depending on Na^+/K^+-ATPase density and input strength, the complete concentration-dependent system exhibits four different regimes: rest, tonic spiking, bursting, and depolarisation block, which have been associated with a range of healthy and/or pathological states. For example, seizures

can be triggered by a handful of neurons going through bursts of activity [53]. In SD, the phase of neuronal hyperactivity preceding the depression can arise from synchronized activity of bursting neurons, as observed by population spikes in electrocorticography (ECoG) traces [54]. In the wave of death (i.e. the massive and simultaneous depolarization of neurons [55]) or when the SD wave changes from hyperactivity to silence, depolarization-block-like dynamics could be observed [51]. The changes in extracellular potassium concentration during bursting and depolarization block in our model are consistent with experimental observations during seizures and SD, as well as during sleep rhythms [56–58].

The SNL bifurcation as an organisational center for bursting

At the core of the present burst mechanism is the SNL bifurcation and the bistable region initiating from it in the fast subsystem. The latter is bounded by the HOM and SN branches, i.e., the two codimension-one bifurcation branches that appear from the codimension-two SNL bifurcation. Interestingly, the majority of seizures observed in patients and experimental models are assumed to rely on an SN/HOM bifurcation [52]. The minimalistic model by Depannemaecker et al. discovered this kind of onset-offset combination (SN/HOM) in their oscillations. Unlike the present model with a one-dimensional slow subsystem, their model features a two-dimensional slow subsystem. Other mechanisms for bursting do not involve SN or HOM bifurcations at the onset and offset of the burst (e.g., [15,16,51,59]).

The SNL bifurcation itself originates from the unfolding of the codimension-3 degenerate Takens–Bogdanov singularity which is present in a large class of conductance-based models [19]. We demonstrate that the minimal bursting mechanism analysed here requires the involvement of the Na^+/K^+-ATPase and ordinary K^+ and Na^+ channels, which are omnipresent throughout the brain.

Proximity of an SNL bifurcation can be found in a generic class of neuron models, i.e. all models starting with class I excitability [21,22], which encompass a significant proportion of neuron models, ranging from isolated gastropod somata to mammalian hippocampal neurons [25]. Note that in the bistable region between the HOM and SN bifurcations, the presence of noise in the system or its input can result in stochastic bursting that emerges from switching between the stable limit cycle attractor and the fixed-point dynamics (see, for example [38]).

Here, in contrast, the bursting mechanism is deterministic and stems from the feedback mediated by the Na^+/K^+-ATPase. Specifically, the electrogenic pump induces a distortion of the bifurcation diagram of the fast subsystem, which is crucial for the actual occurrence of deterministic bursting. If the pump, however, is not included in the voltage dynamics (as, for example, in [15,60,61]), a shear-induced hysteresis loop is not observed.

The relevance of potassium homeostasis

The dynamics described in this study does not explicitly consider other ionic transporters, or external potassium regulators, such as diffusion, or glial cells [16,17,62–66]. The model's extracellular space can, however, be interpreted as an effective compartment that also subsumes possible additional potassium homeostasis mechanisms. Hence, the pathological dynamics introduced in our mechanism could arise from anomalies in these kinds of regulators. This hypothesis is consistent with the experimental observation that dysfunctional astrocytes are crucial players in epilepsy, assuming that extracellular potassium homeostasis is impaired as a function of the astrocytic impairment [67]. Other experiments have implicated dysfunctional astrocytes in SD [68]. We note that although our model produces intriguing dynamics at the level of a single cell, it cannot generate some of the more complex behaviours, such as recovery

from depolarization block. This recovery requires the explicit involvement of other potassium regulators [17], exceeding the scope of this paper.

Relation to previous findings

Our study demonstrates that the interplay between potassium dynamics and neuronal excitability in class I neuron models with SNIC dynamics can give rise to slow bursting under minimal conditions. The general idea of generating diverse spiking dynamics via feedback from increased extracellular potassium has been previously reported and is supported by experimental evidence. For example, fluctuations in extracellular potassium levels have been observed to co-vary with the electroencephalogram (EEG) and field-potential waves during sleep or seizures [56,57,69]. Increases in extracellular potassium have been reported during pathological conditions like seizures and spreading depression [70–72]. Moreover, prior studies have shown that accumulated extracellular potassium does not rapidly diffuse away from neurons, thereby providing a feedback signal that can influence neuronal dynamics [73–77].

On the modelling side, a number of studies have explored the generation of slow deterministic bursting involving changes in ion concentrations. Sætra et al. [78] employed a Pinsky-Rinzel model to highlight the significance of considering ionic concentration dynamics, diffusion, and electrical drift. Bazhenov et al. [12] showed that increasing extracellular potassium levels, alongside various currents triggers rhythmic activity in both individual cells and networks. Also, Kager et al. [44], reported a slow bursting activity (around 0.06 Hz), arising from the interplay of potassium and sodium concentration dynamics in a complex multi-compartmental model with dendrites and glia. In contrast, Øyehaug et al. [59] utilized a similar model but attributed the slow oscillatory behaviour to the slow dynamics of glial cells.

In two papers, Hübel et al. [16,17] demonstrated that the Na^+/K^+-ATPase pump alone is insufficient to recover the system from depolarization block (referred to as free energy-starvation). Through complete system bifurcation analysis, they revealed that models augmented solely with the pump as a homeostatic regulator and within certain ranges of pump strengths, exhibit bistability between physiological states and depolarization block. They further showed that adding another ionic regulatory mechanism, such as a bath or glia, to the model can restore the system from depolarization block back to physiological conditions after a significant phase space excursion in ionic variables. The bistability between physiological cell state and a state of free energy starvation, i.e., depolarisation block, studied in their work, also exists in our model. It is important to note, firstly, that this bistability is different from the bistability in the fast subsystem that the burst mechanism relies on, and secondly, that the free energy depleted depolarisation block, a property of the whole system, is not the same as the Hopf curve in our fast bifurcation diagram, which also terminates spiking. Barreto et al. [15] developed a model incorporating sodium and potassium concentrations as slow subsystems but no pump current in the voltage equation. Their model is capable of producing slow-wave bursting particularly with very high variations in concentration, notably extracellular potassium. Prior to this work, Cressman et al. [60] examined a similar model. By sketching the bifurcation diagram of their slow subsystem, they investigated the effect of different potassium homeostasis (specially bath diffusion and glia) mechanisms on their model. Building upon a similar framework, Wei et al. [51] aimed to enhance the realism of neuron modelling by introducing additional elements such as more realistic glial ionic currents, oxygen and volume dynamics, and the Goldman–Hodgkin–Katz formalism. As a result, their model exhibited a diverse spectrum of dynamics including steady-state, seizure, spreading depression, tonic firing, and wave of death. Depannemaecker et al. [52], in turn, presented a more minimalistic model in which the potassium concentration in the bath compartment is regulated by diffusion. Dependent on the

bath's potassium concentration, this model can generate diverse rhythms. The majority of previous modelling work, however, has predominantly focused on ion-channel-based mechanisms with channel dynamics slower than those typically required for spike generation. Alternatively, concentration dynamics paired with fast spike generating channels were augmented by additional features like multiple compartments or homeostasis mechanisms. In contrast to some earlier studies on bursting induced by ionic concentration [15,60], which required multiple slow variables (termed slow-wave burst [9,19]), our model demonstrates that a single slow concentration ($[K^+]_{out}$) suffices for burst formation. This type of burst is categorised as a hysteresis loop burst [9,19]. In our model, two conditions need to be met for the hysteresis loop to form: First, a bistable region must be part of the bifurcation structure, which is typical for the SNL unfolding in class I neurons. Second, the bifurcation structure must be arranged such that the slow variable can traverse the saddle-node and HOM branches that delimit the bistable region, to respectively initiate and terminate spiking. In our model, this tuning is achieved through the electrogenic action of the ubiquitous Na^+/K^+-ATPase. Due to the universality of the identified mechanism, which applies to any neuron with class I excitability, our results demonstrate the sufficiency of the Na^+/K^+-ATPase for the generation of slow rhythmic bursting across a large set of neuronal cell types.

Summary

In summary, we present a minimal mechanism for deterministic bursting activity that arises from the interplay of very common spiking dynamics with changes in the extracellular potassium concentration mediated by a ubiquitous Na^+/K^+-ATPase. While other, more complex models, exhibit deterministic bursting too, the mechanism described in this study relies only on a minimal set of physiological assumptions in neurons and its dynamics agree with experimental observations in pathological states like epilepsy or spreading depolarization. The underlying mechanism strengthens the role of Na^+/K^+-ATPases in the generation of slow rhythms and their relevance as a therapeutic target in pathology. While more complex models may capture bursting dynamics faithfully, the minimal model enabled us to deduce the exact mechanism involved in the bursting sequence. We anticipate that this detailed understanding, as well as the efficiency of the model in numerical simulations, will facilitate analyses aimed at mechanistically linking the biophysics of neurons to the behaviour of the networks that embed them.

Methods

Model description

In the following, we describe the parsimonious biophysical model, composed only of two fast spike-generating currents and a Na^+/K^+-ATPase pump as well as extracellular potassium concentration ($[K^+]_{out}$) dynamics.

Our model is based on the Wang-Buzsáki model [79]. As it is shown in Fig 1, the model consists of two compartments: the neuron and its extracellular space. The outward potassium current through the neuron's voltage-dependent channels will increase the concentration of $[K^+]_{out}$. Conversely, $[K^+]_{out}$ is decreased by the Na^+/K^+-ATPase pump activity. We calculated these changes by the mass conservation equation of $[K^+]_{out}$. Variation in $[K^+]_{out}$ affects the reversal potential of the potassium, which is calculated by the Nernst equation.

The Wang-Buzsáki model. The Wang-Buzsáki (WB) model is a modified version of the famous Hodgkin-Huxley (HH) model. However, contrary to the HH model for invertebrate motoneurons, the WB model is categorized as a class I neuron model, mimicking fast-spiking vertebrate interneurons dynamics. The model has two fast spike-generating sodium and potassium voltage-dependent channels [79]. The potassium and sodium currents are described

below:

$$I_{Na} = g_{Na} h m_{\infty}^{3} (V - E_{Na}), \tag{1}$$

$$I_{K} = g_{K} n^{4} (V - E_{k}), \tag{2}$$

where the sodium channel inactivation variable h and potassium channel activation variable n are defined with the following equations:

$$\frac{dh}{dt} = 5(\alpha_h(1-h) - \beta_h h) where \begin{cases} \beta_h = \dfrac{1}{\left(exp\left(\dfrac{-28-V}{10}\right)+1\right)}, \\ \alpha_h = 0.07 exp\left(\dfrac{-V-58}{20}\right) \end{cases} \tag{3}$$

$$\frac{dn}{dt} = 5(\alpha_n(1-n) - \beta_n n)\ where \begin{cases} \beta_n = 0.125 exp\left(\dfrac{-V-44}{80}\right)) \\ \alpha_n = \dfrac{(-34-V)}{\left(100\left(exp\left(\dfrac{-34-V}{10}\right)-1\right)\right)} \end{cases}. \tag{4}$$

$$m_{\infty} = \frac{\alpha_m}{(\alpha_m + \beta_m)} where \begin{cases} \alpha_m = \dfrac{(-35-V)}{\left(10\left(exp\left(\dfrac{-35-V}{10}\right)-1\right)\right)}. \\ \beta_m = 4 exp\left(\dfrac{-V-60}{18}\right) \end{cases} \tag{5}$$

Within the framework of the Wang-Buzsáki model, the activation variable of the transient sodium current (m) is considered to evolve rapidly and is thus replaced with its corresponding steady-state function.

This approach serves as a means to simplify the WB model, transitioning it from a four-dimensional system to a three-dimensional one.

The Wang-Buzsáki model also has a leak current, which is described below:

$$I_{L} = g_{L}(V - E_{L}). \tag{6}$$

All of the symbols and constants of this section are described in Table 1.

Na^+/K^+-ATPase pump current. To generate action potentials in neurons, the presence of ionic gradients between the intracellular and extracellular spaces is required. This entails a high concentration of K^+ within the cell and a low concentration outside, while Na^+ is kept at a low concentration within the cell and a high concentration outside. To maintain the resting potential and neuronal excitability the cell membrane contains pumps like the Na^+/K^+-ATPase. The ATPase pump puts 3 sodium ions out of the cells while pumping 2 potassium ions into the cells; hence, this pump is not electroneutral. The concentration dependence of the pump current is a sigmoidal function, adapted from Hübel et al. [17] and modified to match our model so that the resting potential of the Wang-Buzsáki model does not change dramatically:

$$I_{P} = \frac{I_{max}}{\left(1 + exp\left(10 - \frac{[K^+]_{out}}{1.1}\right)\right)}. \tag{7}$$

Table 1. Nomenclature.

Symbol	*Name*	*Value (unit)*
$[K^+]_{out}$	*extracellular potassium concentration*	*variable (mM)*
α *and* β	*gating variables*	*variable* (ms^{-1})
A_{cell}	*surface area of the cell*	3.142×10^{-6} (cm^2) [80]
C	*membrane capacitance*	1 ($\mu F/cm^2$) [79]
E_k	*potassium reversal potential*	*variable (mV)*
E_L	*leak reversal potential*	*-65 (mV)* [79]
E_{Na}	*sodium reversal potential*	*55 (mV)* [79]
F	*Faraday's constant*	9.694×10^4 *(C/mol)* [80]
g_k	*potassium conductance*	*9 (mV)* [79]
g_L	*leak conductance*	*0.1* (mS/cm^2) [79]
g_{Na}	*sodium conductance*	*35* (mS/cm^2) [79]
h	*sodium channel inactivation*	*variable* ___
I_K	*potassium current*	*variable* ($\mu A/cm^2$)
I_L	*leak current*	*variable* ($\mu A/cm^2$)
I_P	Na^+/K^+*-ATPase pump current*	*variable* ($\mu A/cm^2$)
I_{app}	*injected (stimulation) current*	*varies per simulation* ($\mu A/cm^2$)
I_{max}	Na^+/K^+*-ATPase pump maximal current*	*varies per simulation* ($\mu A/cm^2$)
I_{Na}	*sodium current*	*variable* ($\mu A/cm^2$)
m_∞	*fast sodium channel activation*	*variable* ___
n	*potassium channel activation*	*variable* ___
r_v	*ratio of extracellular to intracellular volumes*	*0.15* ___ [80]
t	*time*	*variable (ms)*
V	*membrane potential*	*variable (mV)*
V_{cell}	*cellular volume*	5.23×10^{-10} (cm^3) [80]

https://doi.org/10.1371/journal.pcbi.1011751.t001

This pump equation demonstrates the adaptability of the pump current in response to changes in extracellular potassium concentration. The more potassium has accumulated outside of the cell, the stronger the pump current that pumps potassium back inside. Nevertheless, the pump's current never exceeds the maximum level, I_{max}, set by the density of pumps in the membrane.

Membrane potential equation. Having described all the currents of our model, we can now calculate the membrane potential dynamics as below:

$$C\frac{dV}{dt} = I_{app} - I_{Na} - I_K - I_L - I_P, \tag{8}$$

where I_{app} is the constant applied current or stimulus.

Ionic continuity equation. Neuronal activity raises the potassium reversal potential, while lowering the sodium reversal potential. In general, the sodium reversal potential has a strong impact on action potential height, while the potassium reversal potential induces bifurcations of the resting state and the saddle that determines the threshold manifold. In particular, homoclinic connections to the saddle are affected by changes in potassium reversal potential [38]. Furthermore, due to higher potassium conductance than sodium conductance at the resting potential, the resting membrane potential is typically closer to the potassium reversal potential. Additionally, due to the smaller extracellular space in relation to intracellular space, changes in extracellular potassium concentration ($[K^+]_{out}$) can have a greater effect on

neuronal behaviour than any other neuronal concentration [60]. Therefore, it is reasonable to focus on extracellular potassium dynamics in our model.

For converting the potassium current to potassium ionic flux, we multiply the pump current by two; as in each pumping cycle, two potassium cations are exchanged. Thus, the continuity equation of $[K^+]_{out}$ is as follows:

$$\frac{d[K^+]_{out}}{dt} = \frac{(I_K - 2I_p)A_{cell}}{r_v F V_{cell}}. \tag{9}$$

In our model, the reversal potential of potassium (in Eq 2) is dynamic and is calculated according to the Nernst equation [17,80]:

$$E_k = 26.71 ln\left(\frac{[K^+]_{out}}{140}\right). \tag{10}$$

Dynamic intracellular sodium. To demonstrate that the slow burst dynamics observed in our model is persistent, we have added sodium concentration dynamics to the model. The results of this addition are reported in the Supplement materials (S3 Fig).

The extracellular sodium concentration is higher than the intracellular sodium concentration ($[Na^+]_{in}$). Additionally, the Na^+/K^+-ATPase is responsive to changes in $[Na^+]_{in}$. Hence, to enhance our model with sodium dynamics, we can focus on integrating the dynamics of $[Na^+]_{in}$.

For simulating the model with dynamics $[Na^+]_{in}$, we add the continuity equation for $[Na^+]_{in}$ to the model:

$$\frac{d[Na^+]_{in}}{dt} = \frac{(-I_{Na} - 3I_p)A_{cell}}{F V_{cell}}. \tag{11}$$

We also calculate the reversal potential of sodium with the equation below instead of using it as a parameter:

$$E_{Na} = 26.71 ln\left(\frac{144}{[Na^+]_{in}}\right). \tag{12}$$

Finally, we use the complete model of the pump [17] with some modifications:

$$I_p = \frac{I_{max}}{\left(1 + exp\left(10 - \frac{[K^+]_{out}}{1.1}\right)\right)\left(1 + exp\left(\frac{25 - [Na^+]_{in}}{3}\right)\right)}. \tag{13}$$

To reproduce the bursting pattern shown in Fig 2A, we need to set $[Na^+]_{in}$ to approximately 18.4 mM. Using this concentration in Eq 12 results in E_{Na} = 55 mV, which aligns with our previous simulations. Moreover, in Eq 13 I_{max} should be adjusted. With $[Na^+]_{in}$ near 18.4 mM, I_{max} should be around 10 μA/cm^2. This adjustment allows us to simulate the model under conditions almost identical to those used to generate the results in Fig 2A.

The outcome of the simulation incorporating all the modifications above is presented in S3A Fig. With the $[Na^+]_{in}$ oscillation around 18.4 mM, we successfully replicate the nearly identical bursting dynamics showcased in Fig 2A. However, it is worth noting the presence of a gradual drift in the sodium concentration.

For another sanity check, in the modified model with dynamic $[Na^+]_{in}$, we set $[Na^+]_{in}$ = 18.4 mM. The outcome of this simulation is depicted in S3B Fig, showcasing identical results

to those seen in Fig 2A. Hence, the burst dynamics described in this paper can manifest in more complicated systems.

Slow-fast method

The deterministic bursting introduced in this paper results from the interaction between dynamics on different timescales. First, the fast spiking timescale mostly determined by gating variables of channels and the membrane time constant (Eqs 3, 4 and 8). Second, the slower timescale of the concentration dynamics. The slow dynamics is represented by variation in $[K^+]_{out}$ (Eq 9).

To gain a better understanding of our system's behaviour, we analysed our neuron model using the method of timescale separation [9,26]. For this, one needs to assume that slow and fast timescales are sufficiently separated. As a result, the fast subsystem perceives the slow subsystem ($[K^+]_{out}$) dynamics as a constant parameter. On the other hand, the oscillations of the spiking dynamics are so fast for $[K^+]_{out}$ dynamics that it only senses the average changes in the fast subsystem. By using this strategy, we can consider the fast and slow subsystems separately.

For the fast subsystem, we treat $[K^+]_{out}$ in the system of equations including Eqs 3, 4 and 8, as a bifurcation parameter. Then with the help of numerical continuation [81], we produce the bifurcation diagram of the fast subsystem. This is how we generated Figs 3, 5C, 5D, 6A, 7B and S1.

To analyse the slow subsystem, we apply a numerical averaging method to obtain the reduced slow subsystem [9,18]. The time evolution of the slow subsystem ($[K^+]_{out}$) is given by Eq 9. Actually, the slow subsystem does not respond to the fast changes in the fast subsystem during the spiking phase but only perceives the average effect of each action potential. Therefore, for each desirable $[K^+]_{out}$, we can average the terms that relate to the fast subsystem (I_P and I_K in Eq 9) over one full action potential limit cycle, as shown below:

$$\frac{d[K^+]_{out}}{dt} = \frac{A_{cell}}{FV_{ex}\tau}\int_0^{\tau} (I_K - 2I_p)_{fast}\,dt, \tag{14}$$

where τ is the period of the fast subsystem's limit cycle and the subscript "fast" shows that I_P and I_K belong to the fast subsystem in specific $[K^+]_{out}$.

For each spiking branch of the fast subsystem, we discretize the $[K^+]_{out}$ range that the branch covers and compute the $[K^+]_{out}$ derivative with the averaging method (Eq 14) for each $[K^+]_{out}$ value. This allows us to calculate the reduced system for each spiking branch of the fast subsystem.

When the fast subsystem is quiescent and on its stable fixed point, to determine the slow subsystem dynamics, it is enough to take, at the desired $[K^+]_{out}$, the fast subsystem's fixed-point value of I_P and I_K and put it in Eq 9.

The result of the averaging method as reduced slow subsystem time derivative diagrams are shown in Figs 4, 6B, 6C and 7C.

The averaging method usually breaks down if the time scale difference between the slow and fast subsystems becomes too small. This situation can arise near the fast subsystem bifurcations, such as in the vicinity of the HOM bifurcation, where the spiking frequency is significantly reduced [26]. Hence, in these situations, we validate our results with numerical simulations to ensure the accuracy of our results.

Numerical implementation

We performed numerical simulations using Python 3 [82] and the Brian 2 package [83]. The Runge-Kutta fourth-order method was utilized with time steps of 0.005 ms, and in certain

instances, adaptive time steps were employed. In case of fixed time step method, we verified the results with smaller time steps, which yielded consistent outcomes. Additionally, we carried out the continuation of the bifurcation diagrams using XPPAUT [81] and Auto-07p [84].

Supporting information

S1 Fig. An overview of the bursting dynamics analysis. In the main manuscript, the extracellular potassium concentration ($[K^+]_{out}$) is a variable of special interest, and for consistency, all bifurcations and slow subsystem dynamics are depicted with $[K^+]_{out}$ on the y-axis. Here, we present the dynamic analysis of the burst (Figs 3B and 4) in the more conventional way (with the independent variable $[K^+]_{out}$ on the x-axis). Additionally, we include a more complete depiction of the fast subsystem bifurcation. (**A**) A zoom out of Fig 3B is illustrated here. The bistable region between the saddle-node (SN) and homoclinic (HOM) bifurcation is the bursting region (indicated by the dotted rectangular). Note that there is another bistable region between HOM and Hopf bifurcations where a stable node and a stable limit cycle coexist. According to the slow subsystem dynamics, $[K^+]_{out}$ increases if the fast subsystem spikes. On the stable branch of the fast subsystem emerging from SN bifurcation, [K+]out decreases. From the Hopf bifurcation of the fast subsystem, another stable node is added to the fast subsystem. If the fast subsystem is on this stable node, the complete system dynamics dictates an increase of the $[K^+]_{out}$. (**B**) Phase portrait of the complete burst (as a function of $[K^+]_{out}$ horizontally and voltage vertically, black line giving the trajectory) overlaid with the one-parameter ($[K^+]_{out}$) bifurcation diagram of the fast subsystem (coloured symbols and lines). The bursting trajectory is identical to that in Fig 2A; the diagram corresponds to Fig 3B with flipped axes. Additionally, V_{min} of the stable limit cycle (lower green line) and the unstable focus (dashed purple line) are depicted. (**C**) Hysteresis loop of the slow subsystem overlaid with the bifurcations of the fast subsystem. The $[K^+]_{out}$ dynamics of the reduced, slow subsystem entails a hysteresis loop oscillator. The slow oscillation organises around the bistable region of the fast subsystem, as also shown in panels A and B. The red and blue lines represent the location of the saddle-node (SN) and homoclinic (HOM) bifurcations of the fast subsystem as a function of $[K^+]_{out}$, respectively. This diagram corresponds to Fig 4 with flipped axes. For more information on how to calculate the reduced slow subsystem see Methods (Slow-fast method), and Fig 4 in the main manuscript.
(PDF)

S2 Fig. Jump-on canard at the transition between 11-spike bursts and 12-spike bursts. The spike-adding mechanism at play in our model appears to involve canard solutions. We show here a jump-on canard, found at the transition between the 11-spike burst that was used as illustrative example throughout this paper (Figs 2–4), and a 12-spike burst obtained when increasing the pump density I_{max}. Jump-on canards are particular solutions that connect a fast and attractive component (here when the neurons spikes), to a slow and repulsive component of the dynamics (here the short pause in the spiking within the burst), see for example [85,86]. (**A**) Voltage trace during one period. (**B**) Potassium trace during one period. (**C**) Voltage trajectory superimposed onto the bifurcation diagram of the fast subsystem with respect to potassium. This trajectory follows for a while the repelling slow manifold defined by the saddle point of the fast subsystem involved in the homoclinic bifurcation (orange dashed line). I_{app} = 0.5 μA/cm^2, I_{max} = 0.99450852625 μA/cm^2.
(PDF)

S3 Fig. Effect of intracellular sodium on bursting dynamic. The bursting mechanism introduced in this paper is not affected by the dependence of the Na+/K+-ATPase on $[Na^+]_{in}$. (**A**)

Voltage and ionic concentration dynamics during bursting in a modified model with dynamic $[Na^+]_{in}$. Despite the addition of $[Na^+]_{in}$ dynamics, the bursting described in this paper is still observed, with extracellular potassium accumulating during spiking and decreasing during rest, similar to the behaviour shown in Fig 2. ($I_{app} = 0.5$ μA/cm^2, $I_{max} = 10$ μA/cm^2.) (**B**) Bursting dynamics for the modified model with fixed $[Na^+]_{in}$. By fixing $[Na^+]_{in}$ at 18.4 mM (mean approximation from A) in the modified model, the bursting dynamic is the same as what is depicted in the main model of this paper (see Fig 2).
(PDF)

Acknowledgments

We thank Robert Gowers and Philipp Norton for valuable feedback on the manuscript.

Author Contributions

Conceptualization: Mahraz Behbood, Jan-Hendrik Schleimer, Susanne Schreiber.

Data curation: Mahraz Behbood, Louisiane Lemaire.

Formal analysis: Mahraz Behbood, Louisiane Lemaire.

Funding acquisition: Susanne Schreiber.

Investigation: Mahraz Behbood, Louisiane Lemaire, Jan-Hendrik Schleimer, Susanne Schreiber.

Methodology: Jan-Hendrik Schleimer.

Software: Mahraz Behbood.

Supervision: Jan-Hendrik Schleimer, Susanne Schreiber.

Visualization: Louisiane Lemaire.

Writing – original draft: Mahraz Behbood, Jan-Hendrik Schleimer, Susanne Schreiber.

Writing – review & editing: Mahraz Behbood, Louisiane Lemaire, Jan-Hendrik Schleimer, Susanne Schreiber.

References

1. Marder E, Calabrese RL. Principles of rhythmic motor pattern generation. Physiol Rev. 1996; 76: 687–717. https://doi.org/10.1152/physrev.1996.76.3.687 PMID: 8757786
2. Ramirez J-M, Tryba A, Peña F. Pacemaker neurons and neuronal networks: An integrative view. Curr Opin Neurobiol. 2005; 14: 665–74. https://doi.org/10.1016/j.conb.2004.10.011 PMID: 15582367
3. Debanne D. The Nodal Origin of Intrinsic Bursting. Neuron. 2011; 71: 569–570. https://doi.org/10.1016/j.neuron.2011.08.001 PMID: 21867874
4. Dreier JP, Major S, Pannek H-W, Woitzik J, Scheel M, Wiesenthal D, et al. Spreading convulsions, spreading depolarization and epileptogenesis in human cerebral cortex. Brain. 2012; 135: 259–275. https://doi.org/10.1093/brain/awr303 PMID: 22120143
5. Höller Y, Trinka E. Is There a Relation between EEG-Slow Waves and Memory Dysfunction in Epilepsy? A Critical Appraisal. Front Hum Neurosci. 2015; 9. Available: https://www.frontiersin.org/articles/10.3389/fnhum.2015.00341
6. Brunel N, Wang X-J. What Determines the Frequency of Fast Network Oscillations With Irregular Neural Discharges? I. Synaptic Dynamics and Excitation-Inhibition Balance. J Neurophysiol. 2003; 90: 415–430. https://doi.org/10.1152/jn.01095.2002 PMID: 12611969
7. Kole MHP. First Node of Ranvier Facilitates High-Frequency Burst Encoding. Neuron. 2011; 71: 671–682. https://doi.org/10.1016/j.neuron.2011.06.024 PMID: 21867883

8. Selverston AI, Moulins M. Oscillatory Neural Networks. Annu Rev Physiol. 1985; 47: 29–48. https://doi.org/10.1146/annurev.ph.47.030185.000333 PMID: 2986532

9. Izhikevich EM. Neural excitability, spiking and bursting. Int J Bifurc Chaos. 2000; 10: 1171–1266.

10. Dhamala M, Jirsa VK, Ding M. Transitions to Synchrony in Coupled Bursting Neurons. Phys Rev Lett. 2004; 92: 028101. https://doi.org/10.1103/PhysRevLett.92.028101 PMID: 14753970

11. Samengo I, Mato G, Elijah DH, Schreiber S, Montemurro MA. Linking dynamical and functional properties of intrinsically bursting neurons. J Comput Neurosci. 2013; 35: 213–230. https://doi.org/10.1007/s10827-013-0449-5 PMID: 23575806

12. Bazhenov M, Timofeev I, Steriade M, Sejnowski TJ. Potassium Model for Slow (2–3 Hz) In Vivo Neocortical Paroxysmal Oscillations. J Neurophysiol. 2004; 92: 1116–1132. https://doi.org/10.1152/jn.00529.2003 PMID: 15056684

13. Wang X-J. Neural Oscillations. In: Nadel L, editor. Encyclopedia of Cognitive Science. Chichester: John Wiley & Sons, Ltd; 2006. p. s00343. https://doi.org/10.1002/0470018860.s00343

14. Ramirez JM, Koch H, Garcia AJ, Doi A, Zanella S. The role of spiking and bursting pacemakers in the neuronal control of breathing. J Biol Phys. 2011; 37: 241–261. https://doi.org/10.1007/s10867-011-9214-z PMID: 22654176

15. Barreto E, Cressman JR. Ion concentration dynamics as a mechanism for neuronal bursting. J Biol Phys. 2011; 37: 361–373. https://doi.org/10.1007/s10867-010-9212-6 PMID: 22654181

16. Hübel N, Dahlem MA. Dynamics from Seconds to Hours in Hodgkin-Huxley Model with Time-Dependent Ion Concentrations and Buffer Reservoirs. PLOS Comput Biol. 2014; 10: e1003941. https://doi.org/10.1371/journal.pcbi.1003941 PMID: 25474648

17. Hübel N, Schöll E, Dahlem MA. Bistable Dynamics Underlying Excitability of Ion Homeostasis in Neuron Models. PLOS Comput Biol. 2014; 10: e1003551. https://doi.org/10.1371/journal.pcbi.1003551 PMID: 24784149

18. Rinzel J, Lee YS. On Different Mechanisms for Membrane Potential Bursting. In: Othmer HG, editor. Nonlinear Oscillations in Biology and Chemistry. Berlin, Heidelberg: Springer; 1986. pp. 19–33. https://doi.org/10.1007/978-3-642-93318-9_2

19. Saggio ML, Spiegler A, Bernard C, Jirsa VK. Fast–Slow Bursters in the Unfolding of a High Codimension Singularity and the Ultra-slow Transitions of Classes. J Math Neurosci. 2017; 7: 7. https://doi.org/10.1186/s13408-017-0050-8 PMID: 28744735

20. Hodgkin AL. The local electric changes associated with repetitive action in a non-medullated axon. J Physiol. 1948; 107: 165–181. https://doi.org/10.1113/jphysiol.1948.sp004260 PMID: 16991796

21. Rinzel J, Ermentrout GB. Analysis of neural excitability and oscillations. Methods Neuronal Model. 1998; 2: 251–292.

22. Kirst C, Ammer J, Felmy F, Herz A, Stemmler M. Fundamental Structure and Modulation of Neuronal Excitability: Synaptic Control of Coding, Resonance, and Network Synchronization. bioRxiv. 2015. https://doi.org/10.1101/022475

23. Guckenheimer J, Labouriau JS. Bifurcation of the Hodgkin and Huxley equations: A new twist. Bull Math Biol. 1993; 55: 937–952. https://doi.org/10.1007/BF02460693

24. Kirst C. Synchronization, Neuronal Excitability, and Information Flow in Networks of Neuronal Oscillators. Georg-August-University Göttingen. 2012. https://doi.org/10.53846/goediss-2923

25. Hesse J, Schleimer J-H, Schreiber S. Qualitative changes in phase-response curve and synchronization at the saddle-node-loop bifurcation. Phys Rev E. 2017; 95: 052203. https://doi.org/10.1103/PhysRevE.95.052203 PMID: 28618541

26. Izhikevich EM. Dynamical Systems in Neuroscience: The Geometry of Excitability and Bursting. The MIT Press; 2006. https://doi.org/10.7551/mitpress/2526.001.0001

27. Schleimer J-H, Hesse J, Contreras SA, Schreiber S. Firing statistics in the bistable regime of neurons with homoclinic spike generation. Phys Rev E. 2021; 103: 012407. https://doi.org/10.1103/PhysRevE.103.012407 PMID: 33601551

28. Schleimer J-H, Schreiber S. Phase-response curves of ion channel gating kinetics. Math Methods Appl Sci. 2018; 41: 8844–8858. https://doi.org/10.1002/mma.5232

29. Chow S-N, Lin X-B. Bifurcation of a homoclinic orbit with a saddle-node equilibrium. Differ Integral Equ. 1990; 3: 435–466.

30. Nowacki J, Osinga HM, Tsaneva-Atanasova K. Dynamical systems analysis of spike-adding mechanisms in transient bursts. J Math Neurosci. 2012; 2: 7. https://doi.org/10.1186/2190-8567-2-7 PMID: 22655748

31. Barrio R, Ibáñez S, Pérez L, Serrano S. Classification of fold/hom and fold/Hopf spike-adding phenomena. Chaos Interdiscip J Nonlinear Sci. 2021; 31: 043120. https://doi.org/10.1063/5.0037942 PMID: 34251261

32. Terman D. Chaotic Spikes Arising from a Model of Bursting in Excitable Membranes. SIAM J Appl Math. 1991; 51: 1418–1450. https://doi.org/10.1137/0151071

33. Terman D. The transition from bursting to continuous spiking in excitable membrane models. J Nonlinear Sci. 1992; 2: 135–182. https://doi.org/10.1007/BF02429854

34. Innocenti G, Morelli A, Genesio R, Torcini A. Dynamical phases of the Hindmarsh-Rose neuronal model: Studies of the transition from bursting to spiking chaos. Chaos Interdiscip J Nonlinear Sci. 2007; 17: 043128. https://doi.org/10.1063/1.2818153 PMID: 18163792

35. Linaro D, Champneys A, Desroches M, Storace M. Codimension-Two Homoclinic Bifurcations Underlying Spike Adding in the Hindmarsh—Rose Burster. SIAM J Appl Dyn Syst. 2012; 11: 939–962. https://doi.org/10.1137/110848931

36. Desroches M, Krupa M, Rodrigues S. Spike-adding in parabolic bursters: The role of folded-saddle canards. Phys Nonlinear Phenom. 2016; 331: 58–70. https://doi.org/10.1016/j.physd.2016.05.011

37. Carter P. Spike-Adding Canard Explosion in a Class of Square-Wave Bursters. J Nonlinear Sci. 2020; 30: 2613–2669. https://doi.org/10.1007/s00332-020-09631-y

38. Contreras SA, Schleimer J-H, Gulledge AT, Schreiber S. Activity-mediated accumulation of potassium induces a switch in firing pattern and neuronal excitability type. PLOS Comput Biol. 2021; 17: e1008510. https://doi.org/10.1371/journal.pcbi.1008510 PMID: 34043638

39. Thomas RC. Electrogenic sodium pump in nerve and muscle cells. Physiol Rev. 1972; 52: 563–594. https://doi.org/10.1152/physrev.1972.52.3.563 PMID: 4555514

40. Larsen BR, Stoica A, MacAulay N. Managing Brain Extracellular K+ during Neuronal Activity: The Physiological Role of the Na+/K+-ATPase Subunit Isoforms. Front Physiol. 2016; 7: 141. https://doi.org/10.3389/fphys.2016.00141 PMID: 27148079

41. Xiong Z-Q, Stringer JL. Sodium Pump Activity, Not Glial Spatial Buffering, Clears Potassium After Epileptiform Activity Induced in the Dentate Gyrus. J Neurophysiol. 2000; 83: 1443–1451. https://doi.org/10.1152/jn.2000.83.3.1443 PMID: 10712471

42. Kueh D, Barnett WH, Cymbalyuk GS, Calabrese RL. Na+/K+ pump interacts with the h-current to control bursting activity in central pattern generator neurons of leeches. Griffith LC, editor. eLife. 2016; 5: e19322. https://doi.org/10.7554/eLife.19322 PMID: 27588351

43. Sharples SA, Parker J, Vargas A, Milla-Cruz JJ, Lognon AP, Cheng N, et al. Contributions of h- and Na+/K+ Pump Currents to the Generation of Episodic and Continuous Rhythmic Activities. Front Cell Neurosci. 2022; 15. Available: https://www.frontiersin.org/articles/10.3389/fncel.2021.715427

44. Kager H, Wadman WJ, Somjen GG. Simulated Seizures and Spreading Depression in a Neuron Model Incorporating Interstitial Space and Ion Concentrations. J Neurophysiol. 2000; 84: 495–512. https://doi.org/10.1152/jn.2000.84.1.495 PMID: 10899222

45. Clapcote SJ, Duffy S, Xie G, Kirshenbaum G, Bechard AR, Rodacker Schack V, et al. Mutation I810N in the alpha3 isoform of Na+,K+-ATPase causes impairments in the sodium pump and hyperexcitability in the CNS. Proc Natl Acad Sci U S A. 2009; 106: 14085–14090. https://doi.org/10.1073/pnas.0904817106 PMID: 19666602

46. Hosseinzadeh Z, Hauser S, Singh Y, Pelzl L, Schuster S, Sharma Y, et al. Decreased Na+/K+ ATPase Expression and Depolarized Cell Membrane in Neurons Differentiated from Chorea-Acanthocytosis Patients. Scientific Reports. Springer Science and Business Media LLC; 2020. https://doi.org/10.1038/s41598-020-64845-0 PMID: 32439941

47. Balestrino M, Young J, Aitken P. Block of (Na+,K+)ATPase with ouabain induces spreading depression-like depolarization in hippocampal slices. Brain Res. 1999; 838: 37–44. https://doi.org/10.1016/s0006-8993(99)01674-1 PMID: 10446314

48. Dreier JP. The role of spreading depression, spreading depolarization and spreading ischemia in neurological disease. Nat Med. 2011; 17: 439–447. https://doi.org/10.1038/nm.2333 PMID: 21475241

49. Wei Y, Ullah G, Ingram J, Schiff SJ. Oxygen and seizure dynamics: II. Computational modeling. J Neurophysiol. 2014; 112: 213–223. https://doi.org/10.1152/jn.00541.2013 PMID: 24671540

50. Ingram J, Zhang C, Cressman JR, Hazra A, Wei Y, Koo Y-E, et al. Oxygen and seizure dynamics: I. Experiments. J Neurophysiol. 2014; 112: 205–212. https://doi.org/10.1152/jn.00540.2013 PMID: 24598521

51. Wei Y, Ullah G, Schiff SJ. Unification of Neuronal Spikes, Seizures, and Spreading Depression. J Neurosci. 2014; 34: 11733–11743. https://doi.org/10.1523/JNEUROSCI.0516-14.2014 PMID: 25164668

52. Depannemaecker D, Ivanov A, Lillo D, Spek L, Bernard C, Jirsa V. A unified physiological framework of transitions between seizures, sustained ictal activity and depolarization block at the single neuron level. J Comput Neurosci. 2022; 50: 33–49. https://doi.org/10.1007/s10827-022-00811-1 PMID: 35031915

53. Bromfield EB, Cavazos JE, Sirven JI, editors. An Introduction to Epilepsy. West Hartford (CT): American Epilepsy Society; 2006. Available: http://www.ncbi.nlm.nih.gov/books/NBK2508/

54. Somjen GG. Mechanisms of Spreading Depression and Hypoxic Spreading Depression-Like Depolarization. Physiol Rev. 2001; 81: 1065–1096. https://doi.org/10.1152/physrev.2001.81.3.1065 PMID: 11427692

55. Zhou Y, Sheremet A, Kennedy JP, DiCola NM, Maciel CB, Burke SN, et al. Spectrum Degradation of Hippocampal LFP During Euthanasia. Front Syst Neurosci. 2021; 15. Available: https://www.frontiersin.org/articles/10.3389/fnsys.2021.647011 PMID: 33967707

56. Moody WJ, Futamachi KJ, Prince DA. Extracellular potassium activity during epileptogenesis. Exp Neurol. 1974; 42: 248–263. https://doi.org/10.1016/0014-4886(74)90023-5 PMID: 4824976

57. Dufour S, Dufour P, Chever O, Vallée R, Amzica F. In vivo simultaneous intra- and extracellular potassium recordings using a micro-optrode. J Neurosci Methods. 2011; 194: 206–217. https://doi.org/10.1016/j.jneumeth.2010.10.004 PMID: 20951737

58. Müller M, Somjen GG. Na+ and K+ Concentrations, Extra- and Intracellular Voltages, and the Effect of TTX in Hypoxic Rat Hippocampal Slices. J Neurophysiol. 2000; 83: 735–745. https://doi.org/10.1152/jn.2000.83.2.735 PMID: 10669489

59. Øyehaug L, Østby I, Lloyd CM, Omholt SW, Einevoll GT. Dependence of spontaneous neuronal firing and depolarisation block on astroglial membrane transport mechanisms. J Comput Neurosci. 2012; 32: 147–165. https://doi.org/10.1007/s10827-011-0345-9 PMID: 21667153

60. Cressman JR, Ullah G, Ziburkus J, Schiff SJ, Barreto E. The influence of sodium and potassium dynamics on excitability, seizures, and the stability of persistent states: I. Single neuron dynamics. J Comput Neurosci. 2009; 26: 159–170. https://doi.org/10.1007/s10827-008-0132-4 PMID: 19169801

61. Kaihua M, Gu H-G, Zhao Z. Fast–Slow Variable Dissection with Two Slow Variables: A Case Study on Bifurcations Underlying Bursting for Seizure and Spreading Depression. Int J Bifurc Chaos. 2021; 31: 2150096. https://doi.org/10.1142/S0218127421500966

62. Orkand RK, Nicholls JG, Kuffler SW. Effect of nerve impulses on the membrane potential of glial cells in the central nervous system of amphibia. J Neurophysiol. 1966; 29: 788–806. https://doi.org/10.1152/jn.1966.29.4.788 PMID: 5966435

63. Syková E. Extracellular K+ accumulation in the central nervous system. Prog Biophys Mol Biol. 1983; 42: 135–189. https://doi.org/10.1016/0079-6107(83)90006-8 PMID: 6139844

64. KOFUJI P, NEWMAN EA. POTASSIUM BUFFERING IN THE CENTRAL NERVOUS SYSTEM. Neuroscience. 2004; 129: 1045–1056. https://doi.org/10.1016/j.neuroscience.2004.06.008 PMID: 15561419

65. Beckner ME. A roadmap for potassium buffering/dispersion via the glial network of the CNS. Neurochem Int. 2020; 136: 104727. https://doi.org/10.1016/j.neuint.2020.104727 PMID: 32194142

66. Byvaltcev E, Behbood M, Schleimer J-H, Gensch T, Semyanov A, Schreiber S, et al. KCC2 reverse mode helps to clear postsynaptically released potassium at glutamatergic synapses. Cell Rep. 2023; 42. https://doi.org/10.1016/j.celrep.2023.112934 PMID: 37537840

67. Noebels JL, Avoli M, Rogawski MA, Olsen RW, Delgado-Escueta AV, editors. Jasper's Basic Mechanisms of the Epilepsies. 4th ed. Bethesda (MD): National Center for Biotechnology Information (US); 2012. Available: http://www.ncbi.nlm.nih.gov/books/NBK50785/

68. Seidel JL, Escartin C, Ayata C, Bonvento G, Shuttleworth CW. Multifaceted roles for astrocytes in spreading depolarization: A target for limiting spreading depolarization in acute brain injury? Glia. 2016; 64: 5–20. https://doi.org/10.1002/glia.22824 PMID: 26301517

69. Jensen MS, Yaari Y. Role of Intrinsic Burst Firing, Potassium Accumulation, and Electrical Coupling in the Elevated Potassium Model of Hippocampal Epilepsy. J Neurophysiol. 1997; 77: 1224–1233. https://doi.org/10.1152/jn.1997.77.3.1224 PMID: 9084592

70. Hablitz JJ, Heinemann U. Extracellular K+ and Ca2+ changes during epileptiform discharges in the immature rat neocortex. Dev Brain Res. 1987; 36: 299–303. https://doi.org/10.1016/0165-3806(87)90036-8 PMID: 3690340

71. Haglund MM, Schwartzkroin PA. Role of Na-K pump potassium regulation and IPSPs in seizures and spreading depression in immature rabbit hippocampal slices. J Neurophysiol. 1990; 63: 225–239. https://doi.org/10.1152/jn.1990.63.2.225 PMID: 2313342

72. Florence G, Dahlem MA, Almeida A-CG, Bassani JWM, Kurths J. The role of extracellular potassium dynamics in the different stages of ictal bursting and spreading depression: A computational study. J Theor Biol. 2009; 258: 219–228. https://doi.org/10.1016/j.jtbi.2009.01.032 PMID: 19490858

73. Frankenhaeuser B, Hodgkin AL. The after-effects of impulses in the giant nerve fibres of Loligo. J Physiol. 1956; 131: 341–376. https://doi.org/10.1113/jphysiol.1956.sp005467 PMID: 13320339

74. Baylor DA, Nicholls JG. Changes in extracellular potassium concentration produced by neuronal activity in the central nervous system of the leech. J Physiol. 1969; 203: 555–569. https://doi.org/10.1113/jphysiol.1969.sp008879 PMID: 5387026

75. Rang HP, Ritchie JM. On the electrogenic sodium pump in mammalian non-myelinated nerve fibres and its activation by various external cations. J Physiol. 1968; 196: 183–221. https://doi.org/10.1113/jphysiol.1968.sp008502 PMID: 5653884

76. Singer W, Dieter Lux H. Extracellular potassium gradients and visual receptive fields in the cat striate cortex. Brain Res. 1975; 96: 378–383. https://doi.org/10.1016/0006-8993(75)90751-9 PMID: 1175021

77. Hounsgaard J, Nicholson C. Potassium accumulation around individual purkinje cells in cerebellar slices from the guinea-pig. J Physiol. 1983; 340: 359–388. https://doi.org/10.1113/jphysiol.1983.sp014767 PMID: 6887054

78. Sætra MJ, Einevoll GT, Halnes G. An electrodiffusive, ion conserving Pinsky-Rinzel model with homeostatic mechanisms. PLoS Comput Biol. 2020; 16: e1007661. https://doi.org/10.1371/journal.pcbi.1007661 PMID: 32348299

79. Wang X-J, Buzsáki G. Gamma Oscillation by Synaptic Inhibition in a Hippocampal Interneuronal Network Model. J Neurosci. 1996; 16: 6402–6413. https://doi.org/10.1523/JNEUROSCI.16-20-06402.1996 PMID: 8815919

80. Park E-H, Durand DM. Role of potassium lateral diffusion in non-synaptic epilepsy: A computational study. J Theor Biol. 2006; 238: 666–682. https://doi.org/10.1016/j.jtbi.2005.06.015 PMID: 16085109

81. Ermentrout B. Simulating, analyzing, and animating dynamical systems: a guide to XPPAUT for researchers and students. Philadelphia: Society for Industrial and Applied Mathematics; 2002.

82. Van Rossum G, Drake FL. Python 3 Reference Manual. Scotts Valley, CA: CreateSpace; 2009.

83. Stimberg M, Brette R, Goodman DF. Brian 2, an intuitive and efficient neural simulator. Skinner FK, editor. eLife. 2019; 8: e47314. https://doi.org/10.7554/eLife.47314 PMID: 31429824

84. Continuation and bifurcation software for ordinary differential equations. AUTO-07P; Available: https://github.com/auto-07p/auto-07p

85. Diener M. The canard unchainedor how fast/slow dynamical systems bifurcate. Math Intell. 1984; 6: 38–49. https://doi.org/10.1007/BF03024127

86. De Maesschalck P, Dumortier F, Roussarie R. Canard-cycle transition at a fast–fast passage through a jump point. Comptes Rendus Math. 2014; 352: 27–30. https://doi.org/10.1016/j.crma.2013.09.002